Processes governing the mass balance of Chhota Shigri Glacier (Western Himalaya, India) assessed by point-scale surface energy balance measurements

M. F. Azam[1,2], **P. Wagnon**[1,3], **C. Vincent**[4], **AL. Ramanathan**[2], **V. Favier**[4], **A. Mandal**[2] and **J. G. Pottakkal**[2]

[1] IRD/UJF – Grenoble I/CNRS/G-INP, LGGE UMR 5183, LTHE UMR 5564, 38402 Grenoble Cedex, France

[2] School of Environmental Sciences, Jawaharlal Nehru University, New Delhi 110067, India

[3] ICIMOD, GPO Box 3226, Kathmandu, Nepal

[4] UJF – Grenoble I/CNRS, LGGE UMR 5183, 38041 Grenoble Cedex, France

Correspondence to: M. F. Azam (farooqaman@yahoo.co.in, farooq.azam@lgge.obs.ujf-grenoble.fr)

Abstract

Some recent studies revealed that Himalayan glaciers have been shrinking at an accelerated rate since the beginning of the 21st century. However the climatic causes for this shrinkage remain unclear given that surface energy balance studies are almost nonexistent in this region. In this study, a point-scale surface energy balance analysis was performed using in-situ meteorological data from the ablation zone of Chhota Shigri Glacier over two separate periods (August 2012 to February 2013 and July to October 2013) in order to understand the response of mass balance to climatic variables. Energy balance numerical modeling provides quantification of the surface energy fluxes and identification of the factors affecting glacier mass balance. The model was validated by comparing the computed and observed ablation and surface temperature data. During the summer-monsoon period, net radiation was the primary component of the surface energy balance accounting for 80% of the total heat flux followed by turbulent sensible (13%), latent (5%) and conductive (2%) heat fluxes. A striking feature of the energy balance is the positive turbulent latent heat flux, suggesting re-sublimation of moist air at the glacier surface, during the summer-monsoon characterized by relatively high air temperature, high relative humidity and a continual melting surface. The impact of the Indian summer monsoon on Chhota Shigri Glacier mass balance has also been assessed. This analysis demonstrates that the intensity of snowfall events during the summer-monsoon plays a key role on surface albedo (melting is reduced in case of strong snowfalls covering the glacier area), and thus is among the most important drivers controlling the annual mass balance of the glacier. The summer-monsoon air temperature, controlling the precipitation phase (rain versus snow and thus albedo), counts, indirectly, also among the most important drivers.

1 Introduction

Himalayan glaciers, located on Earth's highest mountain range, are source to numerous rivers that cater to the water needs of millions of people in Asia (e.g., Kaser et al., 2010; Immerzeel et al., 2013). Recent studies have reported negative mass balances over Himalayan glaciers (e.g., Bolch et al., 2012; Kääb et al., 2012; Gardelle et al., 2013), in line with the observation that the Himalayan glaciers (22,800 km^2) have been shrinking at an accelerated rate since the beginning of 21st century (Bolch et al., 2012). Glacial retreat and significant mass loss may not only cause natural hazards such as landslides and glacier lake outburst floods but also increase the specter of shrinking water resources in the long term (Thayyen and Gergan, 2010; Immerzeel et al., 2013).

2

1   Unfortunately, data on recent glacier changes in the Himalayan region are sparse and even
2   sparser as we go back in time (Cogley, 2011; Bolch et al., 2012) and, thus, the rate at which these
3   glaciers are changing remains poorly constrained (Vincent et al., 2013). The erroneous statement
4   in the Intergovernmental Panel on Climate Change (IPCC) Fourth Assessment Report (Parry et
5   al., 2007) about the future of the Himalayan glaciers dragged the attention of the scientific
6   community towards the behavior of these glaciers in relation to climate. However, the IPCC Fifth
7   Assessment Report (Stocker et al., 2013) stated "Several studies of recent glacier velocity change
8   (Azam et al., 2012; Heid and Kääb, 2012) and of the worldwide present-day sizes of accumulation
9   areas (Bahr et al., 2009) indicate that the world's glaciers are out of balance with the present
10   climate and thus committed to losing considerable mass in the future, even without further changes
11   in climate". A reliable prediction of the responses of Himalayan glaciers towards future climatic
12   change and their potential impacts on the regional population requires a sound understanding of
13   the existing physical relationship between these glaciers and climate. This relationship can be
14   addressed in detail by studying the glacier surface energy balance (hereafter SEB).

15   Comprehensive glacier SEB studies began in the early 1950s (e.g., Hoinkes, 1953) and
16   since then our understanding of glacier-climate relationship substantially improved. SEB studies
17   of the world's glaciers and ice sheets have been carried out extensively in the Alps (e.g., Klok and
18   Oerlemans, 2002; Oerlemans and Klok, 2002), Antarctica (e.g., Favier et al., 2011; Kuipers
19   Munneke et al., 2012), Greenland (e.g., Van den Broeke et al., 2011), and the tropics (e.g., Wagnon
20   et al., 1999, 2001, 2003; Favier et al., 2004; Sicart et al., 2005, 2011, Nicholson et al., 2013). In
21   the High Mountain Asia, only a few studies have been carried out mainly in Tian Shan (Li et al.,
22   2011), Qilian mountains (Sun et al., 2014), Tibetan Plateau (Fujita and Ageta, 2000; Yang et al.,
23   2011; Mölg et al., 2012; Zhang et al., 2013) and the Nepalese Himalaya (Kayastha et al., 1999;
24   Lejeune et al., 2013). Glacier SEB studies from Indian Himalaya (covering Western as well parts
25   of Central and Eastern Himalaya) are not yet available. Such SEB studies are crucial because
26   glaciers across the Himalayan range have different mass balance behaviors (Gardelle et al., 2013),
27   depending on their different climatic setup. For example, glaciers in Nepal receive almost all their
28   annual precipitation from the Indian summer monsoon (ISM), and are summer-accumulation type
29   glaciers (Ageta and Higuchi, 1984; Wagnon et al., 2013), while glaciers in Western Himalaya
30   receive precipitation both from the ISM in summer and from mid-latitude westerlies (MLW) in
31   winter (Shekhar et al., 2010).

In this paper, we present a SEB analysis for Chhota Shigri Glacier, Western Himalaya. This glacier is one of the best studied glaciers in Indian Himalaya in terms of mass balance. The first mass balance measurement on this glacier was performed in 1987. Unfortunately, it was abandoned in 1989 and restarted in 2002 (Ramanathan, 2011). Between 2002 and 2013, annual field measurements revealed that the glacier lost mass at a rate of 0.59 ± 0.40 m w.e. a^{-1} (Ramanathan, 2011; Azam et al., 2014). The volume change of Chhota Shigri Glacier has also been measured between 1988 and 2010 using in-situ geodetic measurements by Vincent et al. (2013), revealing a moderate mass loss over this 2 decade-period (-3.8 ± 2.0 m w.e. corresponding to -0.17 ± 0.09 m w.e. a^{-1}). Combining the latter result with field measurements and digital elevation models differencing from satellite images, they deduced a slightly positive or near-zero mass balance between 1988 and 1999 ($+1.0 \pm 2.7$ m w.e. corresponding to $+0.09 \pm 0.24$ m w.e. a^{-1}). Further, Azam et al. (2014) reconstructed the annual mass balances of Chhota Shigri Glacier between 1969 and 2012 using a degree-day approach and an accumulation model fed by long-term meteorological data recorded at Bhuntar meteorological station (~50 km south of the glacier, 1092 m a.s.l.) and discussed the mass balance pattern at decadal scale. They also compared the decadal time scale mass balances with meteorological variables and suggested that winter precipitation and summer temperature are almost equally important drivers controlling the mass balance pattern of this glacier. A period of steady state between 1986 and 2000 and an accelerated mass wastage after 2000 were also defined.

Present studies on the climate sensitivity of Western/Indian Himalayan glaciers either come from empirical analysis at decadal time scales (Azam et al., 2014) or based on basic comparison between meteorological variables and the glacier mass balance (Koul and Ganjoo, 2010), emphasizing the lack of physical understanding of the glacier-climate relationship in this region. Therefore, a detailed analysis of the SEB yet remains underway for Western/Indian Himalayan glaciers. Use of Automatic Weather Stations (AWSs) provides the opportunity to obtain long and continuous records of meteorological data and to study the seasonal and inter-annual variations in SEB at point locations (e.g., Oerlemans, 2000; Reijmer and Oerlemans, 2002; Mölg and Hardy, 2004). The present study is focused on the SEB analysis of Chhota Shigri Glacier, using in-situ AWS measurements. It involves two main objectives: (1) analysis of the glacier's micrometeorology, and (2) an analysis of the SEB components along with the change characteristic

of each component so as to give insights into the processes controlling the mass balance at point scale as well as glacier scale.

2. Data and climatic settings

2. 1 Study site and AWSs description

Chhota Shigri Glacier (32.28 N, 77.58 E) is a valley-type, non-surging glacier located in the Chandra-Bhaga river basin of Lahaul and Spiti valley, Pir Panjal range, Western Himalaya (Fig. 1). It lies ~25 km (aerial distance) from the nearest town of Manali. This glacier feeds Chandra River, one of the tributaries of the Indus River system. Chhota Shigri Glacier extends from 6263 to 4050 m a.s.l. with a total length of 9 km and an area of 15.7 km^2 (Wagnon et al., 2007). The main orientation is north in its ablation area, but its tributaries and accumulation areas have a variety of orientations (Fig. 1). The lower ablation area (<4500 m a.s.l.) is covered by debris representing approximately 3.4% of the total surface area (Vincent et al., 2013). The debris layer is highly heterogeneous, from silt size to big boulders exceeding several meters. The snout is well defined, lying in a narrow valley and giving birth to a single pro-glacial stream. The equilibrium line altitude (ELA) for a zero net balance is 4960 m a.s.l. (Wagnon et al., 2007).

This glacier is located in the monsoon–arid transition zone and influenced by two different atmospheric circulation systems: the ISM during summer (July–September) and the Northern Hemisphere MLW during winter (January–April) (e.g., Bookhagen and Burbank, 2010). On Chhota Shigri Glacier, the hydrological year is defined from 1 October to 30 September of the following year (Wagnon et al., 2007). Since, the glacier sometimes experiences some melting even in October, it would have been more appropriate to start the hydrological year at the beginning of November. Nevertheless, for practical reasons (access to the glacier is impossible after mid-October) and in view of the fact that both October and November are usually characterized by a non-significant mass balance, starting the hydrological year at the beginning of October does not change the results.

Two meteorological stations (AWS1 and AWS2) have been operated on Chhota Shigri Glacier (Fig. 1). AWS1 was operated between 12 August 2012 and 4 October 2013, in the middle of ablation zone (4670 m a.s.l.) on an almost horizontal and homogeneous surface while AWS2 is located off-glacier on a Western lateral moraine (4863 m a.s.l.), functioning continuously since 18 August 2009. At AWS1 and AWS2, meteorological variables are recorded as half-hourly means with a 30-sec time step, except for wind direction (half-hourly instantaneous values), and stored

1 in a Campbell CR1000 data logger. AWS1 is equipped with a tripod standing freely on the glacier

2 with wooden plates at the base of its legs and sinks with the melting surface. AWS2 provides pluri-

3 annual meteorological data (from 2009 to 2013) allowing the characterization of the seasons as

4 well as the analysis of the local climatic conditions on Chhota Shigri Glacier. Both AWS1 and

5 AWS2 were checked and maintained every month during the summers (accessibility in winter was

6 not possible). At the glacier base camp (3850 m a.s.l.), an all-weather precipitation gauge with a

7 hanging weighing transducer (Geonor T-200B) has been operating continuously since 7 July 2012

8 (Fig. 1). The Geonor sensor is suitable for both solid and liquid precipitation measurements. Table

9 1 gives the list of meteorological variables used in this study, with the sensor specifications.

10 **2.2 Meteorological data and corrections**

11 Only AWS1 data were used for SEB calculations. During winter, the lower sensors (T_{air}, RH, u)

12 were buried under heavy snowfalls on 18 January 2013, and AWS1 stopped operating completely

13 on 11 February 2013 till 7 July 2013 when the glacier was again accessible and AWS1 could be

14 repaired. To ensure good data quality, the period between 4 and 11 February 2013 was eliminated

15 as this period was supposed to be influenced by near surface snow. Thus, complete data sets of

16 263 days in two separate periods (13 August 2012 to 3 February 2013 and 8 July to 3 October

17 2013) are available for analysis, except SR50A, for which data are also missing from 8 September

18 to 9 October 2012. The records from AWS2 have very few data gaps (0.003%, 0.29%, and 0.07%

19 data gaps over the 4-year period for T_{air}, u and WD, respectively). These gaps were filled by linear

20 interpolation using the adjacent data. Only one long gap exists for LWI data between 18 August

21 2009 and 22 May 2010.

22 Radiation fluxes are directly measured in the field (Table 1) however several corrections

23 were applied to this data before using in the SEB model. Night values of SWI and SWO were set

24 to zero. At high elevation sites, such as Himalaya, measured SWO can be higher than SWI (2.6%

25 of total data here) during the morning and evening time when the solar angle is low because of

26 poor cosine response of the upward-looking radiation (SWI) sensor (Nicholson et al., 2013).

27 Besides, as AWS1 was installed on the middle of the ablation area, the unstable glacier surface

28 during ablation season conceivably gave rise to a phase shift by mast tilt (Giesen et al., 2009).

29 SWO sensor mostly receives isotropic radiation and consequently is much less sensitive to

30 measurement uncertainties of poor cosine response and mast tilt compared to SWI sensor (Van

31 den Broeke et al., 2004). Therefore, SWI is calculated from SWO (raw) and accumulated albedo

1 (α_{acc}) to avoid the impact of the phase shift because of tilting during the daily cycle of SWI and

2 poor cosine response of the SWI sensor during the low solar angles. α_{acc} values were computed

3 (Eq. 1) as the ratio of accumulated SWO (raw) and SWI (raw) over a time-window of 24 hours

4 centered on the moment of observation using the method described in Van den Broeke et al. (2004).

5 The obvious shortcoming of the accumulated albedo method is the elimination of the clear-sky

6 daily cycle in α_{acc} (Van den Broeke et al., 2004).

7
$$\propto_{acc} = \frac{\sum_{24} SWO}{\sum_{24} SWI} \qquad (1)$$

8   A correction has also been applied to long-wave radiations as the air particles between the

9 glacier surface and CNR-4 sensor radiate and influence LWI (underestimation of LWI at the

10 surface) and LWO (overestimation). This generally occurs when T_{air} is higher than 0 °C during the

11 summer-monsoon (July to September). Figure 2a reveals a linear relation between LWO and T_{air}

12 above 0 °C. Measured LWO was often found substantially greater than 315.6 W m^{-2}, which is the

13 maximum possible value for a melting glacier surface. Therefore, a correction can be done using

14 LWO. We adopted the method described by Giesen et al. (2014) and fitted a linear function to the

15 median values of the additional LWO (greater than 315.6 W m^{-2}) for all 0.5 °C T_{air} intervals above

16 0 °C, assuming that the correction is zero at 0 °C. This correction was added to LWI and subtracted

17 from LWO (Fig. 2b) when T_{air} was higher than 0 °C. Corrections have half-hourly values up to 22

18 W m^{-2} for T_{air} of 11 °C. Over all half-hourly periods with T_{air} above 0 °C, the average correction

19 was 6.3 W m^{-2}.

20   In snow- and ice-melt models, cloud cover is investigated by computing 'cloud factors',

21 defined as the ratio of measured and modeled clear-sky solar radiation (Greuell et al., 1997; Klok

22 and Oerlemans, 2002; Mölg et al., 2009). In the present study cloud factor is calculated by

23 comparing SWI with solar radiation at the top of atmosphere (STOA) according to the Eq.: cloud

24 factor = 1.3−1.4*(SWI/STOA) that represents a quantitative cloud cover estimate and ranges

25 between 0 and 1. The values 1.3 (offset) and 1.4 (scale factor) were derived from a simple linear

26 optimization process (Favier et al., 2004). The cloud factor is calculated between 11:00 and 15:00

27 local time (LT) to avoid the shading effect of steep valley walls during morning and evening time.

28 The theoretical value of STOA is calculated for a horizontal plane following Iqbal (1983) and

29 considering the solar constant equal to 1368 W m^{-2}.

2.3 Accumulation and ablation data

The SR50A sensor records the accumulation of snow (decreasing the sensor distance to the surface) or the melting of ice and melting or packing of snow (increasing the sensor distance from the surface) at 4670 m a.s.l. close to AWS1 (Fig. 3). This sensor does not involve an internal temperature sensor to correct for the variations in speed of sound as a function of T_{air}. Without this correction the measured distance may reduce during the evening, which could be misunderstood as a snowfall event (Maussion et al., 2011). Therefore, temperature corrections for the speed of sound were applied to the sensor output using T_{air} recorded at the higher level. Besides, to reduce the noise, a 3-hour moving mean is applied to smooth the SR50A data. During the summer-monsoon on Chhota Shigri Glacier, sporadic snowfall events and follow-up melting may occur within hours. Therefore, the surface height variations from the 3-hour smoothed SR50A data should be calculated over a time interval long enough to detect the true height changes during the snowfalls and short enough to detect a snowfall before melting begins. Given that SR50A measurements have an uncertainty of ±1 cm, an agreement was achieved with a 6-hour time step between smoothed SR50 data to extract surface changes greater than 1 cm.

Point mass balance was measured from ablation stake n° VI located at the same elevation and around 20 m south to AWS1. Frequent measurements, with intervals of some days to a couple of weeks, were made at stake n° VI during summer expeditions. In summer 2012, 3 stake measurements with intervals of 10 to 15 days have been performed from 8 August to 21 September 2012, while in summer 2013, 6 measurements with intervals of 7 to 30 days have been carried out from 8 July to 3 October 2013. By subtracting the snow accumulation assessed from SR50A measurements at AWS1 (assuming a density of 200 kg m^{-3} for accumulated snow), the ablation was derived corresponding to every period between two stake measurements.

2.4 Climatic settings

2.4.1 Characterization of the seasons

In this section, the meteorological conditions on Chhota Shigri Glacier, as derived from the measurements at AWS2, are described. The Himalayan Mountains are situated in the subtropical climate zone, characterized by high annual thermal amplitude, that allows a separation into summer and winter seasons. The general circulation regime over Himalaya is controlled by the Inter-Tropical Convergence Zone (ITCZ) (Bookhagen and Burbank, 2006; 2010). Figure 4 shows the mean annual cycle of monthly T_{air} and RH during the four hydrological years, from 1 October

2009 to 30 September 2013, recorded at AWS2. The standard deviations (STDs) of mean monthly measurements were 7.0 °C and 13% for T_{air} and RH, respectively, indicating that on Chhota Shigri Glacier, T_{air} and RH variations are large enough to characterize pronounced seasonal regimes. A warm summer-monsoon with high relative humidity from June to September and a cold winter season, comparatively less humid, from December to March were identified. Besides, a pre-monsoon from April to May and a post-monsoon from October to November could also be defined.

Daily mean T_{air} ranges between −22.0 and +7.3 °C with a mean T_{air} of −6.0 °C for the studied cycle (1 October 2009 to 30 September 2013), reflecting the high altitude of the AWS2 location (4863 m a.s.l.). The coldest month was January with a mean T_{air} of −15.8 °C and the warmest month was August with a mean T_{air} of 4.3 °C. Table 2 displays the mean seasonal values of all studied variables for the whole period (1 October 2009 to 30 September 2013). The summer-monsoon is warm (mean T_{air} = 2.5 °C) and calm (mean u = 2.8 m s^{-1}) with high humidity (mean RH = 68%), whereas the winter season is characterized with cold (mean T_{air} = −13.4 °C) and windy (mean u = 5.5 m s^{-1}) conditions with relatively less humidity (mean RH = 42%). The mean annual RH is 52%. An increase (decrease) in mean monthly RH in June (October) shows the onset (end) of monsoon on Chhota Shigri Glacier. Pre-monsoon and post-monsoon seasons showed intermediate conditions for air temperature, moisture and wind speed (Table 2). Although the solar angle is at its annual maximum during the summer-monsoon, SWI is the highest during the pre-monsoon with a mean value of 299 W m^{-2}. The summer-monsoonal mean is 33 W m^{-2} lower than the pre-monsoonal mean because of high cloud coverage in the summer-monsoon. The comparatively low values of SWI, during the summer-monsoon, are compensated by high values of LWI (Fig. 4 and Table 2) mostly emitted from warm summer-monsoonal clouds. Post-monsoon and winter seasons are rather similar, receiving low and almost same SWI (176 and 161 W m^{-2}, respectively) and LWI (187 and 192 W m^{-2}, respectively). The low SWI and LWI values over these seasons are mainly related to the decreasing solar angle (for SWI), and low values of T_{air}, RH and cloudiness (for LWI), respectively.

2.4.2 Influence of ISM and MLW

The whole Himalayan range is characterized by, from west to east, the decreasing influence of the MLW and the increasing influence of the ISM (Bookhagen and Burbank, 2010), leading to distinct precipitation regimes on glaciers depending on their location.

Figure 5 shows the monthly precipitations for a complete hydrological year between 1 October 2012 and 30 September 2013 at Chhota Shigri Glacier base camp (3850 m a.s.l.) (Fig. 1). Surprisingly, the months with minimum precipitation were July to November (mean value of 16 mm) and those with maximum precipitation were January and February (183 and 238 mm, respectively). For ease of understanding, Wulf et al. (2010) divided the distribution of precipitation over the same region in two periods i.e. from May to October with precipitation predominantly coming from ISM and from November to April with precipitation coming from MLW. ISM contributed only 21% while MLW added 79% precipitation to the annual precipitation (976 mm) at Chhota Shigri base camp for 2012/2013 hydrological year. In Fig. 5, a comparison of 2012/2013 monthly precipitation at base camp is also done with long-term (1969-2013) mean monthly precipitations at Bhuntar meteorological station, Beas basin (Fig. 1). Although this station is only about 50 km (aerial distance) from Chhota Shigri Glacier, the precipitation regime is noticeably different because ISM and MLW equally contribute to the average annual precipitation (916 mm yr^{-1}). The different precipitation regimes in this region can be explained by the location of the orographic barrier which ranges between 4000 and 6600 m in elevation (Wulf et al., 2010). ISM, coming from Bay of Bengal in the southeast, is forced by the orographic barrier to ascend, enhancing the condensation and cloud formation (Bookhagen et al., 2005). Thus, it provides high precipitation on the windward side of the orographic barrier at Bhuntar meteorological station (51% of the annual precipitation) and low precipitations on its leeward side at Chhota Shigri Glacier (21% of annual precipitation). In contrast to the ISM, MLW moisture derived from the Mediterranean, Black, and Caspian seas is transported at higher tropospheric levels (Weiers, 1995). Therefore, the winter westerlies predominantly undergo orographic capture at higher elevations in the orogenic interior providing high precipitations at Chhota Shigri Glacier (79% of annual precipitation) compared to Bhuntar meteorological station on the windward side (49% of annual precipitation). Thus, Chhota Shigri Glacier seems to be a winter-accumulation type glacier receiving most of its annual precipitation during the winter season. This precipitation comparison between glacier base camp and Bhuntar meteorological station is only restricted to 2012/2013 hydrological year, when precipitation records at glacier base camp are available. Long-term precipitation data at glacier site are still required to better understand the relationship between the precipitation regimes prevalent on the southern and northern slopes of Pir Panjal Range.

2.4.3 Representativeness of 2012/2013 hydrological year

1   Given that long-term meteorological data at the glacier are unavailable, the representativeness of

2   the meteorological conditions prevailing during the 2012/2013 hydrological year is assessed at

3   Bhuntar using T_{air} and precipitation data from the Bhuntar meteorological station. Figure 6a shows

4   the comparison of 2012/2013 T_{air} with the long-term mean between 1969 and 2013 at seasonal as

5   well as annual scales. T_{air} in 2012/2013 hydrological year was systematically higher for all seasons

6   (0.5 °C, 0.5 °C and 0.6 °C in winter, pre-monsoon and summer-monsoon, respectively) except for

7   post-monsoon when it was lower (0.4 °C) than the mean seasonal T_{air} over 1969-2013 period. At

8   annual scale, 2012/2013 hydrological year was 0.4 °C warmer with T_{air} close to the 75th percentile

9   of the annual mean T_{air} between 1969 and 2013. Figure 6b compares the precipitation observed

10 during the 2012/2013 hydrological year with the mean over 1969-2013 period. In 2012/2013

11 hydrological year, both ISM (May to October) and MLW (November to April) circulations brought

12 almost equal amount (49 and 51%, respectively) of precipitation at Bhuntar meteorological station.

13 This year the ISM precipitation was equal to the mean ISM precipitation over 1969-2013 whereas

14 MLW precipitation was 5% higher than the mean MLW precipitation over 1969-2013 hydrological

15 years (Fig. 6b); therefore, the annual precipitation for 2012/2013 was found slightly higher (943

16 mm w.e.) than the mean annual precipitation (919 mm w.e.) over 1969-2013 hydrological years.

17 In conclusion, 2012/2013 hydrological year was relatively warmer with slightly higher

18 precipitation compared to the annual means over 1969-2013 period. Especially concerning

19 precipitation, the 2012/2013 hydrological year can be considered as an average year.

20 **3. Methodology: SEB calculations**

21 **3.1 SEB equation**

22 The meteorological data from AWS1 were used to derive the SEB at point-scale. The incoming

23 energy at the glacier surface ($F_{surface}$) is computed following Favier et al. (2011):

24 $$SWI - SWO + LWI - [(1- \varepsilon)\, LWI + \varepsilon\, \sigma\, T_{s\_mod}{}^4] + H + LE = F_{surface} \qquad (2)$$

25 where SWI, SWO and LWI are the incident short-wave, outgoing short-wave and incoming

26 long-wave radiations, respectively and the term in square brackets is the modeled outgoing long-

27 wave radiation (LWO_{mod} hereafter) that was deduced from Stefan-Boltzmann's equation (ε is

28 surface emissivity, assumed to be equal to 1 for snow and ice surfaces and $\sigma = 5.67\ 10^{-8}$ W m^{-2} K^{-}

29 ^{4} is the Stefan-Boltzmann constant) using modeled surface temperature T_{s_mod}. H and LE are the

30 sensible and latent turbulent heat fluxes, respectively. The heat supplied by precipitation on

1 glaciers is insignificant compared to the other fluxes (Oerlemans, 2001) therefore neglected here.

2 The fluxes are assigned a positive value if directed towards the glacier surface or vice versa, except

3 the outgoing radiation terms which are kept positive but assigned a negative sign as they are always

4 directed away from the surface. For model validation, T_{s_mod} was compared to the measured surface

5 temperature (T_{s_obs}) which was derived from measured LWO using the Stefan–Boltzmann equation

6 assuming again that the surface emissivity is unity and that it cannot exceed 273.15 K (section

7 4.3).

8      $F_{surface}$ is the energy available at the surface. Part of the shortwave radiation is actually not

9 available for warming/cooling or melting processes at the surface, because shortwave flux partially

10 penetrates into the snow/ice. Hence, $F_{surface}$ is separated into two terms:

11 $$F_{surface} = G_0 + (1 - a)\,SWN = G_0 + SW_{sub} \tag{3}$$

12   where G_0 is the energy excess or deficit at the surface, SWN (=SWI–SWO) is the net short

13 wave radiation and SW_{sub} is the shortwave radiation penetrating in the ice. In this equation, a is

14 the fractional amount of shortwave radiation that is absorbed in the top layer of the model (at the

15 surface). When the modeled surface temperature, T_{s_mod}, is 0 °C, the positive G_0 values represent

16 the energy available for surface melt (m w.e.). Otherwise, this amount is used to cool/warm the

17 frozen surface and underlying snow/ice, depending on its sign. If the subsurface ice/snow

18 temperature exceeds 0 °C, the corresponding energy excess is converted into melt to block T_{s_mod}

19 at 0 °C, but liquid water is assumed to be retained in the ice. When negative surface heat budget

20 occurs, the subsurface temperature stays at 0 °C until this liquid water storage refreezes, then

21 temperature decreases. This is not the case for the surface layer where liquid water is assumed to

22 runoff and hence not available for refreezing processes any more. Ablation is the sum of melt and

23 sublimation (in m w.e.).

24 **3.2 Conduction into the ice/snow**

25 Considering that the energy conservation in the model is crucial, heat conduction (or conductive

26 heat flux, G) into the ice/snow pack was also considered in the model. Assuming horizontal

27 homogeneity, temperature distribution inside the ice is governed by the thermodynamic energy

28 equation (Bintanja et al., 1997; Picard et al., 2009):

$$\rho C_{p-is} \frac{\partial T(z,t)}{\partial t} = -K_s \frac{\partial^2 T(z,t)}{\partial z^2} + \frac{\partial SW_{sub}(z,t)}{\partial z} \tag{4}$$

where t is the time, z is the coordinate normal to the surface (positive downward), ρ is the snow ($\rho_{snow} = 250$ kg m^{-3}) or ice density ($\rho_{ice} = 910$ kg m^{-3}), $T(z)$ is the ice/snow temperature at depth z, K_s is thermal conductivity, C_{p-is} is specific heat capacity of ice/snow at constant pressure, which depends on temperature [$C_{p-is}(z) = 185 + 7.037\ T(z)$ (Dorsey, 1940)], and $SW_{sub}(z,t) = SWN(t)(1 - a)\ e^{-bz}$ is penetrated shortwave flux at depth z. Bintanja et al. (1997) suggested that a is 0.8 for blue ice and 0.9 for snow. Below the surface, the shortwave flux decreases exponentially with a constant extinction coefficient $b = 2.5$ m^{-1} (Bintanja et al., 1997). Distinct thermal conductivities were considered for ice ($K_{s-ice} = 2.0715$ W m^{-1} K^{-1}) and snow (K_{s-snow}). K_{s-snow} was computed according to Douville et al. (1995), as a function of snow density. Thermal diffusion was computed through an explicit scheme to a depth of 2 m, with a 2 cm layer resolution and a 20-sec time step. Neumann limit condition was assumed at the surface (e.g., Picard et al., 2009). This boundary condition results into the following equation:

$$K_s \frac{\partial T(z,t)}{\partial z} = -F_{surface} \tag{5}$$

when G_0 is not used to produce surface melt; otherwise the right side of this boundary condition equation is -SW$_{sub}$. For initial conditions, we assumed that the ice was exposed (no snow at surface) and temperate (every layer was at 0°C) for both studied periods (in 2012 and in 2013).

3.3 Turbulent fluxes

3.3.1. Turbulent flux calculations

The major characteristic of katabatic flow is the wind speed maximum which is dependent on glacier size, slope, temperature, surface roughness and other forcing mechanisms (Denby and Greuell, 2000). Wind speed, T_{air} and RH were measured at two levels (0.8 and 2.5 m) at AWS1. At AWS1 site, u at the upper level (initially at 2.5m) is always higher (99.6% of all half-hourly data) than that at the lower level (initially at 0.8m). For the turbulent heat flux calculations, the bulk method was used. Denby and Greuell (2000) showed that the bulk method gives reasonable results in the entire layer below the wind speed maximum even in katabatic wind conditions

1 whereas the profile method severely underestimates these fluxes. In turn, the bulk method is

2 applied in our present study as it has already been applied in various studies where katabatic winds

3 dominate (e.g. Klok et al., 2005; Geisen et al., 2014).

4 The bulk method calculates the turbulent fluxes including stability correction. This method

5 is usually used for practical purposes because it allows the estimation of the turbulent heat fluxes

6 from one level of measurement (Arck and Scherer, 2002). In this approach, a constant gradient is

7 assumed between the level of measurement and the surface; consequently, surface values have to

8 be evaluated. The stability of the surface layer is described by the bulk Richardson number, Ri_b

9 (Eq. 5) which relates the relative effects of buoyancy to mechanical forces (e.g., Brutsaert, 1982;

10 Moore, 1983; Oke, 1987):

11
$$Ri_b = \frac{g\frac{(T_{air} - T_{S\_mod})}{(z - z_{0T})}}{T_{air}\left(\frac{u}{z - z_{0m}}\right)^2} = \frac{g(T_{air} - T_{s\_mod})(z - z_{0m})^2}{T_{air}u^2(z - z_{0T})} \qquad (6)$$

12 where z is the level of measurements. T_{air} and u are taken from the upper level (2.5 m) that

13 provides a longer period for investigation. The sensor heights were extracted from SR50A records

14 except during a data gap between 8 September and 9 October 2012. Over this period sensor heights

15 were assumed to be constant and set as 2.5 m, this being AWS1 in free standing position. g is the

16 acceleration of gravity ($g = 9.81$ m s^{-2}). z_{0m} and z_{0T} are the surface roughness parameters (in m)

17 for momentum and temperature, respectively. Assuming that local gradients of mean horizontal u,

18 mean T_{air} and mean specific humidity q are equal to the finite differences between the measurement

19 level and the surface, it is possible to give analytical expressions for the turbulent fluxes (e.g., Oke,

20 1987):

21

22
$$H = \rho\frac{C_P k^2 u\left(T_{air} - T_{s\_mod}\right)}{\left(In\frac{z}{z_{0m}}\right)\left(In\frac{z}{z_{0T}}\right)}(\Phi_m\ \Phi_h)^{-1} \qquad (7)$$

23

24
$$LE = \rho\frac{L_S k^2 u(q - q_s)}{\left(In\frac{z}{z_{0m}}\right)\left(In\frac{z}{z_{0q}}\right)}(\Phi_m\ \Phi_v)^{-1} \qquad (8)$$

25

where ρ is the air density (in kg m^{-3}) at 4670 m a.s.l. at AWS1 and calculated using ideal gas equation ($\rho = \frac{P_{atm}}{R_a T}$, where R_a being the specific gas constant for dry air and P_{air} is given by the measurements and around 565 hPa). C_P is the specific heat capacity for air at constant pressure ($C_p = C_{pd}$ (1 + 0.84q) with C_{pd} = 1005 J kg^{-1} K^{-1}, the specific heat capacity for dry air at constant pressure), k is the von Karman constant (k = 0.4) and L_s is the latent heat of sublimation of snow or ice (L_s = 2.834 10^6 J kg^{-1}). Furthermore, q is the mean specific humidity (in g kg^{-1}) of the air at the height z and q_s is the mean specific humidity at surface. z_{0T} and z_{0q} are the surface roughness parameters for temperature and humidity, respectively. To compute turbulent fluxes (Eq. 7 and 8), it is assumed that the temperature is equal to T_{s_mod} at z_{0T} and that the air is saturated with respect to T_{s_mod} at z_{0q}. The last assumption helps to calculate surface specific humidity q_s. The non-dimensional stability functions for momentum (Φ_m), for heat (Φ_h) and moisture (Φ_v) can be expressed in terms of Ri_b (e.g., Favier et al., 2011):

For Ri_b positive (stable): $\qquad (\Phi_m \, \Phi_h)^{-1} = (\Phi_m \, \Phi_v)^{-1} = (1 - 5Ri_b)^2$ $\qquad$ (9)

For Ri_b negative (unstable): $\quad (\Phi_m \, \Phi_h)^{-1} = (\Phi_m \, \Phi_v)^{-1} = (1 - 16Ri_b)^{0.75}$ $\qquad$ (10)

The lower and upper limits of Ri_b were fixed at −0.40 and 0.23, respectively beyond which all turbulence is suppressed (Denby and Greuell, 2000; Favier et al., 2011).

3.3.2 Roughness parameters

The aerodynamic (z_{0m}) and scalar roughness lengths (z_{0T} and z_{0q}) play a pivotal role in bulk method as the turbulent fluxes are very sensitive to the choice of these surface roughness lengths (e.g., Hock and Holmgren, 1996; Wagnon et al., 1999). In several studies (e.g., Wagnon et al., 1999; Favier et al., 2004), the surface roughness lengths were all taken to be equal ($z_{0m} = z_{0T} = z_{0q}$) and used as calibration parameters. In the present study, the z_{0m} was calculated assuming a logarithmic profile for wind speed between both the levels of measurements in neutral conditions (e.g., Moore, 1983):

$$z_{0m} = \exp\left(\frac{u_2 \, ln z_1 - u_1 \, ln z_2}{u_2 - u_1}\right) \qquad (11)$$

where u_1 and u_2 are the wind velocities measured at the lower and higher levels z_1 and z_2, respectively. For −0.005 < Ri_b < 0.005 (11% of our total data set, at half-hourly time-step), it was

1   assumed that conditions are neutral, and half-hourly values for z_{0m} were calculated using the Eq.

2   (11). Half-hourly values of z_{0m} were assessed separately for ice and snow surfaces, based on field

3   observations (snow covered surface between 16/09/2012 and 17/01/2013 and ice-covered surface

4   the rest of the time). The z_{0m} was calculated as 0.016 m (with STD of 0.026 m) and 0.001 m (0.003

5   m) for ice and snow surfaces, respectively. During the summer-monsoon, the surface is covered

6   with hummocks and gullies and z_{0m} is large whereas in winter, snow covers all surface

7   irregularities and fills up the gullies (Fig. 3) providing small values of z_{0m}. The ratio between

8   roughness lengths (z_{0m}/z_{0q} and z_{0m}/z_{0T}) depends on the Reynolds number of the flow according to

9   Andreas (1987) polynomials. For high Reynolds numbers (aerodynamically rough flows), the

10   polynomials suggested by Smeets and Van den Broeke (2008) for hummocks were used. The

11   respective mean values obtained for z_{0T} and z_{0q} are identical and equal to 0.004 m over rough icy

12   surfaces, and 0.001 m over smooth snow surfaces. These values are similar to z_{0m} values for snow-

13   smooth surfaces as already observed by Bintanja and Van den Broeke (1995) and lower for icy-

14   rough surfaces as pointed out by many authors (e.g., Andreas, 1987; Hock and Holmgren, 1996;

15   Meesters et al., 1997).

16   **4. Results**

17   **4.1 Analysis of the meteorological conditions at AWS1**

18   In order to understand the seasonal evolution of the physical processes controlling the mass

19   balance of the glacier, different representative periods for various seasons of 60 days duration were

20   selected for inter-seasonal comparisons, based on the meteorological conditions observed in

21   section 2.4 and available dataset at AWS1. The selected representative periods are post-monsoon

22   (1 October 2012 to 29 November 2012), winter (1 December 2012 to 29 January 2013) and the

23   summer-monsoon (8 July 2013 to 5 September 2013). The same length of 60 days of each

24   representative period was chosen for justified comparison among different seasons. Unfortunately

25   data was not available for pre-monsoon. Measurements (T_{air}, RH, u and WD) recorded at the upper

26   level sensors were used for the analysis, since the records from the lower level sensors have longer

27   data gap because of early burial of sensors. A summary of the mean variables measured in different

28   representative periods at AWS1 is given in Table 3.

29   Figure 7 shows the daily averages of T_{air}, u, RH, LWI, LWO, SWI, SWO, STOA, cloud

30   factor, α_{acc} and snow falls for all three representative periods. The meteorological variables show

31   strong seasonality and day-to-day variability. The last panels of Fig. 7 represent the daily snowfall

1 amounts (with a data gap between 1 and 8 October 2012) at AWS1 site extracted from SR50A

2 data (by applying a fresh snow density of 200 kg m^{-3}). Post-monsoon and winter periods are cold

3 with mean T_{air} and T_{s_obs} always far below freezing point (Fig. 7 and Table 3). During post-

4 monsoon period mean u and α_{acc} progressively increased (mean u = 4.7 m s^{-1} and α_{acc} = 0.73) and

5 reached their highest values in winter period (mean u = 4.9 m s^{-1} and α_{acc} = 0.79). α_{acc} remains

6 almost constant in winter period showing the persistent snow cover. Snowfalls in post-monsoon

7 period were frequent but generally very light (<10 mm w.e.), whereas winter period received a

8 substantial amount of snow (the heaviest snowfalls were observed on 16 December 2012, and 17,

9 18 January 2013 with 32, 44 and 80 mm w.e., respectively). These snowfall events are associated

10 with high RH, α_{acc}, cloud factor and LWI values. Obviously, an abrupt decrease of SWI

11 (consequently low SWO) is noticed during snowfall events. Most of the time, due to very cold and

12 dry high-elevation atmosphere, LWI remains very low during both the periods, with mean values

13 of 205 and 189 W m^{-2} in post-monsoon and winter periods, respectively (Table 3). An analysis of

14 Fig. 7 showed that overcast days with high cloud factor, high RH, increased LWI and decreased

15 SWI are evident during all three representative periods.

16 The summer-monsoon period is warm and calm with relatively high humidity (Fig. 7 and

17 Table 3). SWI is high during the summer-monsoon period (however, the maximum SWI is

18 expected in pre-monsoon, section 2.4.1) with a mean value of 248 W m^{-2} (Table 3). Most SWI

19 (81%) is absorbed by the glacier because of the lowest values of α_{acc} (mean value = 0.19)

20 consequently low SWO. The low and almost constant α_{acc} indicates that the glacier ice was exposed

21 all the time. The surface remains almost continuously in melting condition, as shown by constantly

22 maximal LWO values. Although the summer-monsoon period is characterized by the highest value

23 of cloud factor (0.4), few snowfall events are observed from the SR50A at AWS1 site. Given that

24 T_{air} was above freezing point, the precipitation might have occurred in the form of rain most of the

25 time. Due to warm, humid and cloudy conditions, LWI is much higher in the summer-monsoon

26 than during the other two studied seasons, with a mean value of 300 W m^{-2} (Table 3).

27 Post-monsoon and winter periods are characterized by high wind speeds (mean u values of

28 4.7 and 4.9 m s^{-1}, respectively; Table 3). In the summer-monsoon period u is quite stable (STD =

29 0.5 m s^{-1}) and gusts at minimum strength with a mean value of 3.6 m s^{-1}. Chhota Shigri Glacier is

30 situated in an almost north-south oriented valley and the AWS1 site is bounded by steep valley

31 walls to the east and west (Fig 1). The scatter plots of u with T_{air} and WD over all of the observation

periods at half-hourly time scale were plotted following Oerlemans (2010). Figure 8a mostly shows a linear relationship between T_{air} above melting point and u at AWS1 site showing that increasing u is associated with increasing near-surface T_{air}, indicative of katabatic forcing, whereas Fig. 8b reveals a mean down-glacier wind (WD of 200-210°) most of the time.

Wind direction, measured at AWS1, indicates that there is a persistent down-glacier wind coming from south to southwest (200-210°) during post-monsoon and winter periods (Fig. 9). In winter, the half-hourly mean u reaches up to 10 m s^{-1} compared to 8 m s^{-1} in post-monsoon period. During both post-monsoon and winter periods the glacier surface is snow covered (with high α_{acc}, Fig. 7) and a down-glacier wind is maintained by the negative radiation budget (section 4.2) of the snow surface which gives rise to cooling to the near-surface air, generating katabatic flow (Grisogono and Oerlemans, 2002). Further, on Chhota Shigri Glacier, in the summer-monsoon period the wind regime is quite remarkable. During the summer-monsoon, the down-glacier wind, coming from south to southwest (200-210°) is relatively weak and might be the result of katabatic forcing, which is typical for many valley glaciers (Van den Broeke, 1997). Occasionally, wind also tends to come from south-east (160°), in the direction of a large hanging glacier (Fig. 1). The upcoming valley wind coming from north-east (50°), blowing against the down-glacier wind, is weak at the AWS1 site and appears only during the summer-monsoon periods when the down-glacier wind is comparatively weak. As a cumulative result of upcoming valley and down-glacier winds, a wind from 110° is also observed.

AWS1 is surrounded by steep N-S valley walls. In order to analyze the impact of synoptic scale circulation at AWS1 site, we compared the wind directions at AWS1 with those at 450 hPa pressure level obtained from High Asia Reanalysis data (HAR, Maussion et al., 2014) at hourly scale. HAR wind data is available at 10 km resolution for different pressure levels for the 2001-2012 period. The pressure level of 450 hPa (equivalent to ~6350 m a.s.l.) has been chosen as representative of the synoptic circulation above the glacier (whose highest elevation is 6263 m a.s.l.). Synoptic (HAR, 450 hPa) wind comes mainly from west or south-west directions, depending on the season. Given that on its eastern side the glacier is bordered by a high N-S ridge (often above 6000 m a.s.l.), this synoptic wind may be deflected down to the valley providing winds parallel to the katabatic flow at AWS1. Therefore at AWS1 site the wind coming from south to southwest is probably the result of both katabatic and synoptic effects.

4.2 Mean values of the SEB components

Mean SEB values for three representative periods are presented in Fig. 10 and are reported in Table 3. The results indicate that the mean seasonal net short wave radiation (SWN) is highly variable from 29 W m^{-2} in winter to 202 W m^{-2} in the summer-monsoon (Table 3). Besides the seasonal changes in sun inclination, the main reason for the seasonal variability of SWN is the contrast in surface albedo in different periods (Table 3). Seasonal variations in net long wave radiations (LWN=LWI–LWO$_{mod}$) are rather low; post-monsoon and winter periods show minimum values of LWN (mean = –69 and –54 W m^{-2}, respectively), while the maximum was obtained for the summer-monsoon period (mean = –14 W m^{-2}) when T_{s_mod} (mean = –0.2 ^{o}C) remains close to the melting point and coincides with warm and humid conditions associated with dense cloud cover leading to high values of LWI. The net radiation heat flux R (=SWN + LWN) was negative in post-monsoon and winter periods, giving rise to near-surface air cooling, with mean values of –21 and –25 W m^{-2}, respectively whereas in the summer-monsoon, it was the main heat source with a mean value of 187 W m^{-2}. During all representative periods, the atmosphere transported heat towards the glacier surface in the form of H. The highest contribution of H (associated with the highest T_{s_mod}, Table 3) was in the summer-monsoon with a mean value of 31 W m^{-2} (Table 3). LE was continuously negative in post-monsoon and winter periods with mean values of –45 and –27 W m^{-2}, respectively. Therefore, the surface lost mass through sublimation (corresponding to respective mean daily rates of –1.4 and –0.8 mm w.e. d^{-1}). However, in the summer-monsoon period, a sign shift in LE from negative to positive occurred. The relatively high T_{air} and RH (Table 3) lead to a reversal of the specific humidity gradient and therefore a positive LE for a melting valley glacier (Oerlemans, 2000). Because of this positive LE, glacier gained mass through condensation or re-sublimation of moist air at the surface (Table 3). Assuming re-sublimation as the main process an amount of 0.3 mm w.e. d^{-1} mass gain is calculated during the summer-monsoon period. The amount of short-wave radiation penetrating below the surface (SW$_{sub}$) is slightly negative during post-monsoon and winter seasons while in the summer-monsoon it was highest in agreement with the highest values of SWN. When sub-surface ice layers were at 0°C, this energy amount was converted into subsurface melt occurring in the first layer of the model, leading to runoff. At daily time scale, the conductive heat flux (G) was mostly negligible except during the summer-monsoon when it was slightly positive and was responsible for a small energy gain during the night in the upper layers of the glacier, which resulted in melt when these layers were at melting point soon after the sunrise.

1   As a result of SEB, positive melt heat flux ($F_{surface}$), with almost the same seasonal

2   oscillation as SWN (Fig. 10), occurred only in the summer-monsoon period when melting

3   conditions were prevailing all the time, leading to a mean daily melt rate of 61.3 mm w.e. d^{-1}.

4   During the summer-monsoon period SWN accounted for 87% of the total heat flux and was the

5   most important heat-flux component for surface melting. R was estimated as 80% of the total heat

6   flux that was complemented with turbulent sensible, latent and conductive heat fluxes with a share

7   of 13%, 5% and 2%, respectively. During post-monsoon period the glacier started cooling down

8   (mean $F_{surface}$ = −56 W m^{-2}) with a little melting (mean daily rate of 0.6 mm w.e. d^{-1}) occurring

9   during the noon hours only, when occasionally T_{s_mod} reached 0 °C, while in winter period the

10   glacier was too cold (the highest half hourly T_{s_mod} was −4.23 °C) to experience any melting (mean

11   $F_{surface}$ = −24 W m^{-2}).

12   **4.3 Model validation**

13   The model provides a heat transfer at half-hourly time step to the glacier superficial layers that can

14   be turned into melt when the modeled surface temperature, T_{s_mod}, is at 0 °C. When the computed

15   snow or ice temperature exceeds 0°C, the corresponding energy excess is also converted into melt.

16   Sub-surface melt participates to runoff when it occurs in the first layer of the model. Another way

17   to lose/gain mass is from sublimation/re-sublimation. The amount of sublimation/re-sublimation

18   (m w.e.) was computed from calculated LE divided by the latent heat of sublimation (2.834 10^6 J

19   kg^{-1}) and the density of water (1000 kg m^{-3}) when the half-hourly mean LE flux was

20   negative/positive. During the summer-monsoon, glacier lost mass at a daily mean melt rate of 61.3

21   mm w.e. d^{-1}, while a mass gain of 0.3 mm w.e. d^{-1} was observed through re-sublimation (Table 3).

22   Sublimation was negligible during the summer-monsoon.

23   To validate the SEB model, computed ablation (melt + sublimation − re-sublimation) was

24   compared with the ablation measured at stake n° VI in the field (section 2.3). The correlation

25   between computed ablation from the SEB Eq. and measured ablation at stake n° VI is strong (r^2 =

26   0.98, n = 9 periods), indicating the robustness of the model. Although, the computed ablation is

27   1.15 times higher than the measured one (Fig. 11a), this difference (15% overestimation) is

28   acceptable given the overall uncertainty of 140 mm w.e. in stake ablation measurements (Thibert

29   et al., 2008). Furthermore, surface temperatures at half-hourly time step (T_{s_mod}) were calculated

30   by the model without using measured LWO (or associated surface temperatures, T_{s_obs}). Figure

31   11b shows that the half-hourly T_{s_obs} and T_{s_mod} are highly correlated (r^2 = 0.96), with an average

difference of 1.2 $^{\circ}$C. This temperature difference corresponds to a mean difference of 4.6 W m^{-2} between LWO$_{mod}$ and observed LWO, showing that the modeled surface heat budget is reasonably computed. Moreover, if we run the model with an additional 2-cm snow layer at the surface when measured albedo values are higher than 0.7, the mean difference between T_{s_mod} and to T_{s_obs} drops to 0.2°C, showing that this difference does not come from a bad performance of the model, but from a bad estimation of the surface state (snow or ice) and thus of precipitation during low intensity events (explaining the bi-modal scatter observed in Fig. 11b i.e. surface state correctly reproduced or not). Thus when the surface state is appropriately assessed, the model provides a good estimation of T_{s_mod}. In conclusion, given that the model is able to properly compute surface temperature or ablation at point-scale, we believe that it can reasonably calculate all the SEB fluxes.

4.4 Mean diurnal cycle of the meteorological variables and SEB components

The mean diurnal cycles of the meteorological variables and SEB components for all three representative periods are shown in Fig. 12. Mean diurnal cycles of T_{s_mod} (equivalent to LWO$_{mod}$) and T_{air} showed that the glacier was in freezing conditions during post-monsoon and winter periods all the time (Fig. 12) while in the summer-monsoon, T_{s_mod} is always at melting point in agreement with consistently positive T_{air}. Occasionally, for some days, half-hourly mean T_{air} (not shown here) may drop below freezing point during the night in the summer-monsoon and climb above freezing point during noon hours in post-monsoon period. A wind speed maximum is observed in the afternoon hours during all the representative periods, which is consistent with T_{air}. This is a common phenomenon on valley glaciers, with u increasing in the afternoon (e.g., Van den Broeke, 1997; Greuell and Smeets, 2001) as a consequence of an increased glacier wind due to a stronger T_{air} deficit in the afternoon. A wind speed minimum is observed in the morning time of post-monsoon but no reason for this could be identified.

For all the representative periods, R is negative at night (indicating long-wave radiative cooling of the surface) and positive during the day time. However, during the summer-monsoon period the night values of R are slightly less negative as the radiative cooling is attenuated due to enhanced RH, T_{air}, cloudiness, and in turn high LWI. In daytime, R is much higher during the summer-monsoon than other periods, mainly because of exposed low-albedo ice at the glacier surface enhancing the absorption of solar radiation, which is already high due to annual maximum of the solar angle.

1   *H* and LE show similar daily cycles in post-monsoon and winter periods. During the night,

2   *H* remains permanently high (~50 W m^{-2}) and starts decreasing in the morning as the surface is

3   heated up with *R* (Fig. 12). This daily cycle of *H* is in agreement with the daily cycle of Ri_b,

4   showing stable conditions almost all day long ($Ri_b > 0$ except 4 hours in the middle of the afternoon

5   in winter), with very stable conditions in the night, and moderately stable during the day or even

6   unstable in the afternoon in winter. LE is negative in the night, decreases in the morning and shows

7   the minimum values during early afternoon hours which are in agreement with increasing wind

8   speed and stronger vertical gradients of specific humidity in the vicinity of the surface. During the

9   summer-monsoon, both *H* and LE are positive (heat supplied to the surface) and follow a similar

10   trend, but *H* attains its peak approximately 2 hours before LE. *H* shows a peak at ~14:00 LT with

11   positive T_{air} and wind speed maximum (Fig. 12) whereas LE remains close to 0 W m^{-2} until noon

12   and increases with an afternoon wind speed maximum. The stability of the surface boundary layer

13   is not very different from that observed during the other periods, highly stable at night, but

14   moderately stable during the day due to the occurrence of warm up-valley winds blowing over a

15   melting surface in summer-monsoon. Thus, LE is positive during the summer-monsoon giving rise

16   to re-sublimation in afternoon and early night hours.

17   SW$_{sub}$ mirrors the daily cycle of SWN but is attenuated as part of SWN is absorbed by the

18   surface, and part is transferred to the underlying layers, following an exponential extinction.

19   During winter and post-monsoon, negative values of *G* are compensated by positive values in the

20   afternoon (after 16:00 LT, when surface temperature begins to decrease) or early night hours,

21   leading to insignificant values of this heat flux at daily scale. During the summer-monsoon, *G* is

22   equal to zero during daytime and only positive at night when internal layers of the glacier at the

23   melting point try to compensate the nocturnal surface cooling and thus bring energy to the surface.

24   During post-monsoon and winter periods, in the night, $F_{surface}$ is negative, and a cold front

25   penetrates into the superficial layers of the glacier. However, $F_{surface}$ is rather low as *R* is mostly

26   compensated by *H*+LE except during noon hours when $F_{surface}$ switches to slightly positive values.

27   Heat is then transferred during a few hours of the day to the ice/snow pack whose temperature

28   rises but not enough to reach melting conditions (T_{s_mod} remains below 0 °C) (Fig. 12). During the

29   summer-monsoon period, $F_{surface}$ follows the diurnal cycle of *R* providing energy up to 710 W m^{-2}

30   to the glacier surface at around 12:00 LT. This energy is consumed for melting process as the

31   surface is melting continuously (Fig. 12). Unfortunately, the dataset does not cover the pre-

monsoon. But during this season, the heat transferred to the glacier progressively increases as net short-wave radiation enhances in agreement with the rise in solar angle, as well as the decreasing surface albedo. This heat is first used to warm up the surface layers of the glacier until $T_{\text{s\_mod}}$ reaches 0 °C, then melting starts.

5. Discussion

5.1 Control of the summer-monsoon snowfalls on melting

5.1.1 Comparison between 2012 and 2013 melting periods

The impact of ISM has already been analyzed on Tibetan glaciers (e.g., Fujita and Ageta, 2000; Yang et al., 2011; Mölg et al., 2012 & 2014) but it is still not well understood in the Himalaya. Previously, based on a degree-day approach, Azam et al. (2014) suggested that winter precipitation and summer temperature are almost equally important drivers controlling the mass balance pattern of Chhota Shigri Glacier. Here this topic is addressed by analyzing the surface melting on Chhota Shigri Glacier with the summer-monsoon precipitations using more detailed SEB approach. Based on the available dataset, we selected the same length of the summer-monsoon period (15 August to 30 September) from 2012 and 2013 years to compare the evolution of the computed cumulative melting (Fig. 13). Given that the SR50A at AWS1 site has a data gap between 8 September to 9 October 2012 and that this sensor cannot record rain events, daily precipitations, collected at glacier base camp (3850 m a.s.l.), are used in this analysis. These precipitation values are extrapolated at AWS1 assuming a zero-precipitation gradient and are considered as rain (snow) at AWS1 site when T_{air} at AWS1 is above (below) 1 °C (e.g., Wagnon et al., 2009). In the summer-monsoon 2012, Chhota Shigri Glacier received one important snowfall of 25 mm w.e. (equivalent to 125 mm of fresh snow applying a density of 200 kg m^{-3}) during 17-19 September. This snowfall abruptly changed the surface conditions by varying the surface albedo from 0.19 to 0.73 (Fig. 13a). Therefore, the energy F_{surface} available at the glacier surface suddenly dropped from 123 W m^{-2} on 16 September to 14 W m^{-2} on 17 September as shown by the sharp change in the melting rate (slope of the melting curve on Fig. 13a) associated to this specific snowfall event. The effect is also evident on $T_{\text{s\_mod}}$ evolution. The daily number of hours with $T_{\text{s\_mod}} > -1$ °C decreased from 24 to 6 hours and remained around this value throughout, showing that melting, which was continuous before the snowfall event, is reduced to a few hours of the day. During the summer-monsoon 2013, the situation was different as the snowfalls were more sporadic and never big enough to efficiently slow down the melting. Consequently, a shift in the slope in the melting curve

23

1   is not observed as was the case in mid-September 2012. Indeed, the light snowfalls, observed from

2   13 to 16 September 2013 and from 24 to 30 September 2013, were only able to protect the glacier

3   from high melting for some days but could not maintain a persistent snow cover as in mid-

4   September 2012. Ice was again exposed at the surface as revealed by low albedo values (~0.38)

5   observed again a few days after the snowfalls. Mean T_{air} and the daily number of hours with

6    $T_{s\_mod} > -1$ ℃ again rose up, maintaining the high melt rates. As a consequence, at point scale,

7   although the cumulative melting between 15 August and 30 September was very similar in 2012

8   and 2013 (2.08 and 1.96 m w.e., respectively), the main difference comes from the distribution of

9   the melting along the considered period. Although the melt rates in 2012 were higher than 2013

10   during the first 31 days, an early snowfall efficiently slowed down the melting, however it was

11   slightly less intense but more regular in 2013.

12   In order to better quantify the albedo effect of the mid-September 2012 snow falls on the

13   glacier melting, the model was run again assuming a constant albedo (=0.19) over the entire 2012

14   summer period, all other meteorological variables being unchanged meanwhile (Fig. 13a). As

15   expected, the overall melting with constant albedo is enhanced (2.44 m w.e.) with a moderate

16   difference of 0.36 m w.e. (+17% compared to a simulation with real albedo) between 15 August

17   and 30 September 2012, but very significant when considering only the period when the observed

18   albedo differs from 0.19 (i.e. after 17 September 2012). Certainly, between 17 and 30 September,

19   the computed melting using a constant albedo (0.19) is 0.48 m w.e., 4 times higher than that with

20   the observed albedo (0.12 m w.e.). Even though Chhota Shigri Glacier is a winter-accumulation

21   type glacier, this analysis highlights and quantifies the role of snowfall events during the summer-

22   monsoon on albedo and, in turn on melting.

23   This effect has already been described in other parts of the world. Sicart et al. (2011)

24   suggested that melting on Zongo Glacier, Bolivia is reduced by wet season snowfalls via the albedo

25   effect during the melt season. In central Tibetan Plateau, Fujita and Ageta, (2000), Fujita (2008a

26   & 2008b) and Zhang et al. (2013) indicated that the glacier surface mass balance was closely

27   related to the summer-monsoon precipitation seasonality and phase (snow versus rain). Mölg et al.

28   (2012) analyzed the impact of ISM on Zhadang Glacier using their fully distributed SEB/mass

29   balance model between 2009 and 2011 and concluded that the timing of monsoon onset leaves a

30   clear footprint on the glacier via the albedo effect. Recently Mölg et al. (2014) extended this

1   analysis at decadal scale and opined that the intensity of ISM onset together with MLW dynamics

2   are important in determining the annual mass balance of Zhadang Glacier.

3   **5.1.2. Impact of the summer-monsoon snowfalls on glacier-wide mass balance**

4   In order to investigate the impact of the summer-monsoon snowfalls on glacier-wide mass balance,

5   the annual glacier-wide mass balances between 2002 and 2013 were compared with the largest

6   summer-monsoon daily snowfalls of the corresponding season. These snowfalls have been

7   extrapolated using daily precipitation data from Bhuntar meteorological station (1092 m a.s.l.),

8   assuming no precipitation gradient and applying the daily lapse rate between Bhuntar and glacier

9   calculated by Azam et al. (2014) with the idea that if the precipitation is in the form of snow

10   (threshold temperature equal to 1°C) at 4400 m a.s.l. (below 4400 m a.s.l. the glacier is totally

11   debris covered), the whole glacier is covered by summer-monsoonal snow.

12   The choice of using precipitation data from Bhuntar meteorological station to assess

13   precipitation on the glacier might seem unfortunate at first glance because, as already discussed in

14   section 2.4.2., both sites are separated by an orographic barrier inducing a different precipitation

15   distribution. However, these sites are only 50 km away from each other, and we believe that

16   meteorological conditions are not totally decoupled between the windward and the leeward side

17   of the mountain range, especially in the case of precipitation events strong enough to cross this

18   orographic barrier. Fortunately, Wulf et al. (2010) conducted a thorough study using the

19   precipitation data of 80 stations from the northwest Himalaya including Chhota Shigri area and

20   concluded that in Baspa Valley (~100 km southeast to Chhota Shigri Glacier) "The two most

21   prominent 5-day-long erosional events account for 50% of the total 5-year suspended sediment

22   flux and coincide with synoptic scale monsoonal rainstorms. This emphasizes the erosional impact

23   of the ISM as the main driving force for erosion processes in the orogenic interior, despite more

24   precipitation falling during the winter season".

25   The best relationship is obtained when considering the sum of the three most important

26   daily snowfall records of the corresponding summer-monsoon (Fig. 14). The correlation is strong

27   ($r^2 = 0.88$, n = 11 years) and suggests that the summer-monsoon snowfall events play a key role to

28   control the mass balance of the glacier. Such snowfalls cover the whole glacier implying the albedo

29   of the whole ablation area to suddenly switch from low to high values (ice to snow surfaces).

30   Consequently, melting is abruptly reduced or even stopped at the glacier surface for several weeks

31   or even for the rest of the ablation season that usually ends around mid-October in years without

such strong summer-monsoon snowfalls. Thus, the intensity of such summer-monsoon snowfalls is among the most important drivers controlling the annual mass balance of Chhota Shigri Glacier.

Azam et al. (2014), using a degree-day approach, showed that winter precipitation and summer temperature are equally important drivers controlling the glacier-wide mass balance of Chhota Shigri Glacier. This present analysis extends this knowledge a step further, showing that the summer-monsoon snowfalls also play an important role in controlling the annual mass balance of Chhota Shigri Glacier. Indeed, the summer-monsoon air temperature is as crucial as summer precipitation mainly because it controls the amount of rain versus snow received at the glacier surface and in turn, has an important control on glacier albedo and thus on the amount of short-wave radiation absorbed by the glacier surface, which is the main heat source for Himalayan glaciers.

5.2 Comparison of the SEB of Chhota Shigri Glacier with that of other glaciers in the High Mountain Asia

In this section some key features of the energy fluxes responsible for the ablation on glaciers in the High Mountain Asia are discussed in the light of the SEB results obtained on Chhota Shigri Glacier, as well as from some previously published studies. Table 4 shows an up-to-date compilation of SEB studies from the High Mountain Asia glaciers coming from ablation zones of different glaciers during summer ablation periods.

As already highlighted on the High Mountain Asia glaciers (Yang et al., 2011; Mölg et al., 2012; Zhang et al., 2013; Sun et al., 2014), the present study also showed that SWN is the largest source of energy to the glacier surface and mainly controls the temporal variability of melting, whereas LWN is the greatest energy loss, moderate during the summer-monsoon when LWO_{mod} is almost compensated by maximum LWI due to warm, humid and cloudy atmosphere, and high during the rest of the year when LWI reaches minimum values (Fig. 10 and Table 3). SWN is inversely dependent on surface albedo. At AWS1 site on Chhota Shigri Glacier, during the summer-monsoon period, precipitation often occurs in liquid form and surface albedo is relatively constant (Fig. 7). During such conditions SWN is driven by cloud factor (Fig. 7). However when precipitation occurs in solid phase (Fig. 13), the surface albedo abruptly changes and controls the SWN and in turn, melting. Sum of SWN and LWN, R, provides >80% energy flux to the glacier surface during the summer-monsoon for all the High Mountain Asia glaciers (Table 4).

All the studied sites, described in Table 4, are on the debris free ablation area. A negative contribution (in %) is assigned to negative heat fluxes in order to have the resulting flux $F_{surface}$ equal to 100%. Sensible turbulent heat flux is always positive and provides energy to the glacier surface, complementing net radiation flux. However its contribution to R ranges from 7% on Laohugou Glacier No. 12, western Qilian, China, to the maximum of 23% on Zhadang Glacier, central Tibetan Plateau over the corresponding observation periods (Table 4). During the summer-monsoon, LE is positive on Chhota Shigri Glacier due to warm and humid air at the glacier surface, giving rise to re-sublimation at the surface. This phenomenon has already been observed on AX010 Glacier located in an ISM-dominated region, Central Himalaya, Nepal, where Kayastha et al. (1999) measured a positive LE between 25 May and 25 September 1978 in the ablation area. On Parlung Glacier No. 4, southeast Tibetan Plateau, however, the mean LE was slightly negative from 21 May to 8 September 2009 (Table 4), while it was continuously positive with a mean value of 8 W m^{-2} during the core summer-monsoon between 25 June and 21 August 2009 because of the considerably high temperature and relative humidity associated with the summer-monsoon circulation over this period (Table 2 in Yang et al., 2011). Conversely, in the central Tibetan Plateau, where dry conditions prevail, on Zhadang Glacier, LE is continuously negative at monthly scale (Mölg et al., 2012) but at daily time scale it was slightly positive during the core monsoon for a few days when the air temperature and relative humidity were the highest (Fig. 2 and 5 in Zhang et al., 2013). Sun et al. (2014) also showed that on Laohugou Glacier No. 12, Western Qilian Mountains, LE is negative throughout the summer season (1 June to 30 September 2011), and rarely becomes positive (only on 2 and 3 July). Similarly on Xixibangma Glacier, south central Tibetan Plateau, and Keqicar Glacier, southwest Tianshan, LE was found to be negative during the observation period, indicating sublimation. From the present analysis (Table 4), it can be surmised that, on the High Mountain Asia glaciers, sublimation predominates in the summer-monsoon over the ablation zone of the glaciers that are less affected by the ISM and submitted to drier conditions than those directly affected like Chhota Shigri Glacier, where LE brings a significant amount of energy at the glacier surface, in the form of re-sublimation. The conductive heat flux is most of the time negligible compared to the other terms of the SEB, even during the summer-monsoon where it slightly contributed to melt.

6. Conclusion

In the Indian Himalaya where meteorological observations are short and scarce, the meteorological dataset recorded since August 2009 at 4863 m a.s.l. on a lateral moraine of Chhota Shigri Glacier (AWS2) is one of the longest ever recorded datasets at high elevation. Mean monthly meteorological conditions at AWS2 show large month-to-month variability. A warm and calm summer-monsoon with high relative humidity from June to September and a cold and windy winter season with comparatively less humidity from December to March were identified. Besides, a pre-monsoon from April to May and a post-monsoon from October to November with intermediate conditions were also defined. Precipitation records at glacier base camp suggest that Chhota Shigri Glacier is a winter accumulation type glacier receiving around 80% of its annual precipitation from MLW in winter and 20% from ISM; but longer precipitation records at glacier site are still needed to confirm this feature.

A physically-based energy balance experiment, using a model computing surface and sub-surface heat fluxes, was carried out to understand the melting processes on Chhota Shigri Glacier based on the forcing data over two separate periods from 13 August 2012 to 3 February 2013 and from 8 July to 3 October 2013 recorded at an in-situ meteorological station (AWS1, 4670 m a.s.l.) in the ablation zone. The roughness length for momentum was calculated separately for ice and snow surfaces as 0.016 m and 0.001 m, respectively whereas roughness lengths for temperature and humidity were derived from the Reynolds number and the roughness length for momentum. Net short wave radiation was highly variable with the lowest mean value (29 W m^{-2}) in winter to the highest (202 W m^{-2}) in the summer-monsoon period, while net long wave radiation exerted lower seasonality with minimum values in post-monsoon and winter periods (–69 and –54 W m^{-2}, respectively) and maximum in the summer-monsoon period (–14 W m^{-2}). During the summer-monsoon period the melting conditions with high T_{s_mod} (mean = –0.2 $^{\circ}$C) coincides with warm and humid conditions, associated with intense cloud covers, leading to high values of LWI and thus high net long wave radiation is observed. Net all-wave radiation was negative in post-monsoon and winter periods, indicative of radiative cooling of the glacier surface, whereas in the summer-monsoon, it was the main heat source for melting. Through the entire observation period, the atmosphere transported heat towards the glacier surface in the form of sensible heat flux. An interesting feature observed in latent heat flux evolution was it being continuously negative in post-monsoon and winter periods, indicating predominantly sublimation; while in the summer-monsoon period, it switched to positive values indicating re-sublimation at the glacier surface. The

result from the SEB equation suggests that energy was available for melting in the summer-monsoon period only. Net all-wave radiation was the main heat flux towards surface with 80% contribution while H, LE and G shared 13%, 5% and 2% of total heat flux, respectively.

This study highlights the impact of the summer-monsoon snowfalls on glacier mass balance. Snowfall events during the summer-monsoon play an important role on melting via surface albedo. The intensity of these snowfalls during ablation period abruptly changes the surface conditions from ice to snow, slowing down the melting rates. Therefore, these snowfall events are among the most important drivers controlling the annual mass balance of Chhota Shigri Glacier. The summer-monsoon air temperature, controlling the precipitation phase (rain versus snow and thus albedo), also counts indirectly, among the most important drivers for the glacier mass balance.

A comparison of the SEB measured at the ablation zone of Chhota Shigri Glacier with those of other glaciers in the High Mountain Asia shows that net short wave radiation flux is the largest energy source and mainly controls the melt energy to the glacier surface whereas net long wave radiation flux is the greatest energy loss. In the High Mountain Asia, sublimation predominates in the summer-monsoon over the ablation zone of the glaciers less affected by the ISM and submitted to drier conditions than those directly affected like Chhota Shigri Glacier, where LE brings a significant amount of energy at the glacier surface in the form of re-sublimation.

The good validation of the present model (comparison between modeled and observed ablation and surface temperature data) indicates that the model is reliable enough to make robust calculations of surface energy balance. In the upcoming future, this study would be useful to calibrate spatially distributed energy- and mass-balance models at glacier as well as regional scale. These models can be used to predict the future of water supply using different climate change projections.

References

Ageta, Y. and Higuchi, K.: Estimation of mass balance components of a summer-accumulation type glacier in the Nepal Himalaya, Geogr. Ann. A, 66, 249–255, 1984.

Aizen, V. B., Aizen, E. M. and Nikitin S. A.: Glacier regime on the northern slope of the Himalaya (Xixibangma glaciers), Quat. Int., 97–98, 27–39, doi:10.1016/S1040-6182(02)00049-6, 2002.

Andreas, E. L.: A theory for the scalar roughness and the scalar transfer coefficients over snow and sea ice, Bound.-Lay. Meteorol., 38, 159–184, 1987.

Arck, M. and Scherer, D.: Problems in the determination of sensible heat flux over snow. Geogr. Ann. A, 84, 157–169, 2002.

Azam, M. F., Wagnon, P., Ramanathan, AL., Vincent, C., Sharma, P., Arnaud, Y., Linda, A., Pottakkal, J. G., Chevallier, P., Singh, V. B., and Berthier, E.: From balance to imbalance: a shift in the dynamic behaviour of Chhota Shigri Glacier (Western Himalaya, India), J. Glaciol., 58, 315–324, doi:10.3189/2012JoG11J123, 2012.

Azam, M. F., Wagnon, P., Vincent, C., Ramanathan, AL., Linda, A., and Singh, V. B.: Reconstruction of the annual mass balance of Chhota Shigri Glacier (Western Himalaya, India) since 1969, Ann. Glaciol., 55(66), 69-80, doi: 10.3189/2014AoG66A104, 2014.

Bahr, D. B., Dyurgerov, M., and Meier, M. F.: Sea-level rise from glaciers and ice caps: A lower bound, Geophys. Res. Lett., 36, L03501, doi:10.1029/2008GL036309, 2009.

Bintanja, R. and Van den Broeke, M. R.: The surface energy balance of Antarctic snow and blue ice, J. Appl. Meteorol., 34, 902–926, 1995.

Bintanja, R., Jonsson, S. and Knap W.: The annual cycle of the surface energy balance of Antarctic blue ice, J. Geophys. Res., 102(D2), 1867–1881, doi:10.1029/96JD01801, 1997.

1 Bolch, T., Kulkarni, A., Kääb, A., Huggel, C., Paul, F., Cogley, J. G., Frey, H., Kargel, J. S., Fujita,
2 K., Scheel, M., Bajracharya, S., and Stoffel, M.: The State and Fate of Himalayan Glaciers,
3 Science, 336, 310–314, 2012.

4 Bookhagen, B., Thiede, R. C., and Strecker, M. R.: Abnormal monsoon years and their control on
5 erosion and sediment flux in high, arid northwest Himalaya; Earth Planet. Sci. Lett, 231, 131–146,
6 2005.

7 Bookhagen, B. and Burbank, D. W.: Topography, relief, and TRMM-derived rainfall variations
8 along the Himalaya, Geophys. Res. Lett., 33, L08405, doi:10.1029/2006GL026037, 2006.

9 Bookhagen, B. and Burbank, D. W.: Toward a complete Himalayan hydrological budget:
10 Spatiotemporal distribution of snowmelt and rainfall and their impact on river discharge, J.
11 Geophys. Res., 115, F03019, doi:10.1029/2009JF001426, 2010.

12 Brustaert, B.: Evaporation in the Atmosphere: Theory, History and Application, 299, Kluwer
13 Acad., Norwell, Mass, 1982.

14 Cogley, J. G., Kargel, J. S., Kaser, G. and van der Veen, C. J.: Tracking the Source of
15 Misinformation, Science 29 January 2010: 522. DOI:10.1126/science.327.5965.522-a, 2010.

16 Cogley, J. G.: Present and future states of Himalaya and Karakoram glaciers. Ann. Glaciol.,
17 52(59), 69-73, 2011.

18 Denby, B. and Greuell, W.: The use of bulk and profile methods for determining surface heat fluxes
19 in the presence of glacier winds, J. Glaciol., 46, 445–452, 2000.

20 Dorsey, N. E.: Properties of Ordinary Water-Substance in All Its Phases: Water-Vapor, Water, and
21 All the Ices, Reinhold, New York, 1940.

22 Douville, H., Royer, J. F. and Mahfouf, J. F.: A new snow parameterization for the Météo-France
23 climate model, Part I: Validation in standalone experiments, Clim. Dyn., 12, 21–35,
24 doi:10.1007/BF00208760, 1995.

Favier, V., Wagnon, P., Chazarin, J. P., Maisincho, L., and Coudrain, A.: One-year measurements of surface heat budget on the ablation zone of Antizana Glacier 15, Ecuadorian Andes, J. Geophys. Res., 109, D18105, doi:10.1029/2003JD004359, 2004.

Favier, V., Agosta , C., Genthon , C., Arnaud , L., Trouvillez , A., and Gallée , H.: Modeling the mass and surface heat budgets in a coastal blue ice area of Adelie Land, Antarctica, J. Geophys. Res., 116, F03017, doi:10.1029/2010JF001939, 2011.

Fujita, K. and Ageta, Y.: Effect of summer accumulation on glacier mass balance on the Tibetan Plateau revealed by mass-balance model, J. Glaciol., 46, 244–252, 2000.

Fujita, K.: Influence of precipitation seasonality on glacier mass balance and its sensitivity to climate change, Ann. Glaciol, 48, 88-92, 2008a.

Fujita, K.: Effect of precipitation seasonality on climatic sensitivity of glacier mass balance, Earth and Planetary Science Letters, 276, 14–19, 2008b.

Gardelle, J., Berthier, E., Arnaud, Y., Kääb, A.: Region-wide glacier mass balances over the Pamir-Karakoram-Himalaya during 1999–2011, The Cryosphere., 7, 1263-1286, 2013.

Giesen, R. H., Andreassen, L. M., Van den Broeke, M. R., and Oerlemans, J.: Comparison of the meteorology and surface energy balance at Storbreen and Midtdalsbreen, two glaciers in southern Norway, The Cryosphere, 3, 57-74, doi:10.5194/tc-3-57-2009, 2009.

Giesen, R. H., Andreassen, L. M., Oerlemans, J. and Van den Broeke, M. R.: Surface energy balance in the ablation zone of Langfjordjøkelen, an arctic, maritime glacier in northern Norway. J. Glaciol., 60, 57-70, doi: 10.3189/2014JoG13J063, 2014.

Greuell, W., Knap, W. H., and Smeets, P. C.: Elevational changes in meteorological variables along a mid-latitude glacier during summer, J. Geophys. Res., 102(D22), 25941–25954, 1997.

Greuell, W. and Smeets, P.: Variations with elevation in the surface energy balance on the Pasterze (Austria), J. Geophys. Res., 106, 31717–31727, 2001.

Grisogono, B. and Oerlemans, J.: Justifying the WKB approximation in pure katabatic flows, Tellus A 54, 453-463, 2002.

Heid, T. and Kääb, A.: Repeat optical satellite images reveal widespread and long term decrease in land-terminating glacier speeds, The Cryosphere, 6, 467-478, doi:10.5194/tc-6-467-2012, 2012.

Hock, R. and Holmgren, B.: Some aspects of energy balance and ablation of Storglaciaren, Northern Sweden, Geogr. Ann. A, 78, 121–131, 1996.

Hoinkes, H.C.: Measurements of ablation and heat balance on alpine glacier. J. Glaciol., 2, 497–501, 1953.

Immerzeel, W. W., Pellicciotti, F. and Bierkens, M. F. P.: Rising river flows throughout the twenty-first century in two Himalayan glacierized watersheds, Nat. Geosci, 6 (9), 742–745, 2013.

Iqbal, M.: An introduction to solar radiation, Academic Press, New York, 1983.

Kääb, A., Berthier, E., Nuth, C., Gardelle, J. and Arnaud, Y.: Contrasting patterns of early 21st century glacier mass change in the Himalaya, Nature, 488(7412), 495–498, doi:10.1038/nature11324, 2012.

Kaser, G., Großhauser, M. and Marzeion, B.: Contribution potential of glaciers to water availability in different climate regimes, Proc. Natl. Acad. Sci., 107(47), 20223–20227, doi:10.1073/pnas.1008162107, 2010.

Kayastha, R. B., Ohata, T., and Ageta, Y.: Application of mass balance model to a Himalayan glacier, J. Glaciol., 45, 559–567, 1999.

Klok, E. J. L. and Oerlemans, J.: Model study of the spatial distribution of the energy and mass balance of Morteratschgletscher, Switzerland, J. Glaciol., 48, 505–518, 2002.

Klok, E. J., Nolan, M., and Van den Broeke, M. R.: Analysis of meteorological data and the surface energy balance of McCall Glacier, Alaska, USA, J. Glaciol., 51, 451–461, 2005.

Koul, M. N. and Ganjoo R. K.: Impact of inter- and intra-annual variation in weather parameters on mass balance and equilibrium line altitude of Naradu Glacier (Himachal Pradesh), NW Himalaya, India, Clim. Change, 99, 119–139, doi:10.1007/s10584-009-9660-9, 2010.

Kuipers Munneke, P., Van den Broeke, M. R., King, J. C., Gray, T., and Reijmer, C. H.: Near-surface climate and surface energy budget of Larsen C ice shelf, Antarctic Peninsula, The Cryosphere, 6, 353-363, doi:10.5194/tc-6-353-2012, 2012.

Lejeune, Y., Bertrand, J.-M., Wagnon, P., and Morin, S.: A physically based model of the year-round surface energy and mass balance of debris-covered glaciers, J. Glaciol., 59, 327–344, doi:10.3189/2013JoG12J149, 2013.

Li, J., Liu, S., Zhang, Y., and Shangguan, D.: Surface energy balance of Keqicar Glacier, Tianshan Mountains , China , during ablation period, Sciences in Cold and Arid Regions, 3, 197–205, doi: 10.3724/SP.J.1226.2011.00197, 2011.

Marks, D., and Dozier, J.: Climate and energy exchange at the snow surface in the alpine region of the Sierra Nevada, 2, Snow cover energy balance, Water Resour. Res., 28(11), 3043-3054, 1992.

Maussion, F., Wei, Y., Huintjes, E., Pieczonka, T., Scherer, D., Yao, T., Kang, S., Bolch, T., Buchroithner, M., and Schneider, C.: Glaciological field studies at Zhadang Glacier (5500–6095 m), Tibetan Plateau, in: Workshop on the use of automatic measuring systems on glaciers – Extended abstracts and recommendations of the IASC Workshop, edited by: Tijm-Reijmer, C. H. and Oerlemans, J., 23–26 March 2011, Pontresina (Switzerland), 62–68, Institute for Marine and Atmospheric Research, Utrecht University, 2011.

Maussion, F., Scherer, D., Mölg, T., Collier, E., Curio, J. and Finkelnburg, R.: Precipitation Seasonality and Variability over the Tibetan Plateau as Resolved by the High Asia Reanalysis, J. Climate, 27, 1910–1927, doi:10.1175/JCLI-D-13-00282.1, 2014.

Meesters, A. G. C. A., Bink, N. J. H., Vugts, F., Cannemeijer, F. and Henneken , E. A. C.: Turbulence observations above a smooth melting surface on the Greenland Ice Sheet, Boundary Layer Meteorol., 85, 81 – 110, 1997.

Mölg, T. and Hardy, D. R.: Ablation and associated energy balance of a horizontal glacier surface on Kilimanjaro, J. Geophys. Res., 109, 1-13, doi:10.1029/2003JD004338, 2004.

Mölg, T., Cullen, N. J., and Kaser, G.: Solar radiation, cloudiness and longwave radiation over low-latitude glaciers: implications for mass-balance modelling, J. Glaciol., 55, 292–302, doi:10.3189/002214309788608822, 2009.

Mölg, T., Maussion, F., Yang, W., and Scherer, D.: The footprint of Asian monsoon dynamics in the mass and energy balance of a Tibetan glacier, The Cryosphere, 6, 1445–1461, doi:10.5194/tc-6-1445-2012, 2012.

Mölg, T., Maussion, F., and Scherer, D.: Mid-latitude westerlies as a driver of glacier variability in monsoonal High Asia, Nature Climate Change, 4, 68-73, 2014.

Moore, R.: On the use of bulk aerodynamic formulae over melting snow. Nordic Hydrol., 14, 193–206, 1983.

Nicholson, L. I., Prinz, R., Mölg, T., and Kaser, G.: Micrometeorological conditions and surface mass and energy fluxes on Lewis Glacier, Mt Kenya, in relation to other tropical glaciers, The Cryosphere, 7, 1205-1225, doi:10.5194/tc-7-1205-2013, 2013.

Oerlemans, J.: Analysis of a 3 year meteorological record from the ablation zone of Morteratschgletscher, Switzerland: energy and mass balance, J. Glaciol., 46, 571–579, 2000.

Oerlemans, J.: Glaciers and climate change, A. A. Balkema, The Nethrelands, 2001.

Oerlemans, J. and Klok, E.: Energy balance of a glacier surface: analysis of automatic weather station data from Morteratschgletscher, Switzerland, Arct., Antarct. Alp. Res., 34, 477–485, 2002.

Oerlemans J.: The Microclimate of Valley Glaciers. Igitur, Utrecht University, 138 pp., ISBN 987-90-393-5303-5, Utrecht Publishing & Archiving Services, The Netherlands, 2010.

Oke, T. R.: Boundary Layer Climates. Second Edition, Routledge, 423 pp., 1987.

Parry, M. L., Canziani, O. F., Palutikof, J. P., van der Linden, P. J. and Hanson C. E.: Contribution of Working Group II to the Fourth Assessment Report of the Intergovernmental Panel on Climate Change, 2007, Cambridge University Press, Cambridge, United Kingdom and New York, NY, USA, 2007.

Picard, G., Brucker, L., Fily, M., Gallée, H. and Krinner, G.: Modeling time series of microwave brightness temperature in Antarctica, J. Glaciol., 55(191), 537–551, doi:10.3189/002214309788816678, 2009.

Ramanathan, AL.: Status Report on Chhota Shigri Glacier (Himachal Pradesh), Himalayan Glaciology Technical Report No. 1, Department of Science and Technology, Ministry of Science and Technology, New Delhi, 88 pp., 2011.

Reijmer, C. H. and Oerlemans, J.: Temporal and spatial variability of the surface energy balance in Dronning Maud Land, East Antarctica, J. Geophys. Res., 107, 4759–4770, doi:10.1029/2000JD000110, 2002.

Shekhar, M., Chand, H., Kumar, S., Srinivasan, K., and Ganju, A.: Climate-change studies in the western Himalaya, Ann. Glaciol., 51, 105–112, doi:10.3189/172756410791386508, 2010.

Sicart, J. E., Wagnon, P., and Ribstein, P.: Atmospheric controls of the heat balance of Zongo Glacier (16° S, Bolivia), J. Geophys. Res., 110, D12106, doi:10.1029/2004JD005732, 2005.

Sicart, J. E., Hock, R., Ribstein, P., Litt, M., and Ramirez, E.: Analysis of seasonal variations in mass balance and meltwater discharge of the tropical Zongo Glacier by application of a distributed energy balance model, J. Geophys. Res., 116, D13105, doi:10.1029/2010JD015105, 2011.

Smeets, C. J. P. P. and Van den Broeke, M. R.: The parameterisation of scalar transfer over rough ice surfaces, Bound.-Lay. Meteorol., 128, 339–355, 2008.

Stocker, T. F., Qin, D., Plattner, G.-K., Tignor, M., Allen, S. K., Boschung, J., Nauels, A., Xia, Y., Bex, V., and Midgley, P. M.: IPCC: Climate Change 2013: The Physical Science Basis. Contribution of Working Group I to the Fifth Assessment Report of the Intergovernmental Panel on Climate Change, Cambridge University Press, Cambridge, United Kingdom and 10 New York, NY, USA, in press, 2013.

Sun, W., Qin, X., Du, W., Liu, W., Liu, Y., Zhang, T., Xu, Y., Zhao, Q., Wu, J., and Ren, J.: Ablation modeling and surface energy budget in the ablation zone of Laohugou glacier No. 12, western Qilian mountains, China, Ann. Glaciol., 55(66), 111-120, 10.3189/2014AoG66A902, 2014.

Thayyen, R. J. and Gergan, J. T.: Role of glaciers in watershed hydrology: a preliminary study of a "Himalayan catchment", The Cryosphere, 4, 115-128, doi:10.5194/tc-4-115-2010, 2010.

Thibert, E., Blanc, R., Vincent, C., and Eckert, N.: Glaciological and volumetric mass balance measurements: Error analysis over 51 years for Glacier de Sarennes, French Alps, J. Glaciol., 54, 522–532, 2008.

Van den Broeke, M. R.: Momentum, heat and moisture budgets of the katabatic wind layer over a mid-latitude glacier in summer, Journal of Applied Meteorology 36, 763-774, 1997.

Van den Broeke, M. R., Van As, D., Reijmer, C. H., and Van de Wal, R. S. W.: Assessing and Improving the Quality of Unattended Radiation Observations in Antarctica, J. Atmos. Ocean. Tech., 21, 1417–1431, 2004.

Van den Broeke, M. R., Smeets, C. J. P. P., and Van de Wal, R. S. W.: The seasonal cycle and interannual variability of surface energy balance and melt in the ablation zone of the west Greenland ice sheet, The Cryosphere, 5, 377-390, doi:10.5194/tc-5-377-2011, 2011.

Vincent, C., Ramanathan, Al., Wagnon, P., Dobhal, D. P., Linda, A., Berthier, E., Sharma, P., Arnaud, Y., Azam, M. F., Jose, P. G., and Gardelle, J.: Balanced conditions or slight mass gain of glaciers in the Lahaul and Spiti region (northern India, Himalaya) during the nineties preceded recent mass loss, The Cryosphere, 7, 569-582, doi:10.5194/tc-7-569-2013, 2013.

Wagnon, P., Linda, A., Arnaud, Y., Kumar, R., Sharma, P., Vincent, C., Pottakkal, J. G., Berthier, E., Ramanathan, A., Hasnain, S. I., and Chevallier, P.: Four years of mass balance on Chhota Shigri Glacier, Himachal Pradesh, India, a new benchmark glacier in the western Himalaya, J. Glaciol., 53, 603–611, 2007.

Wagnon, P., Ribstein, P., Francou, B., and Pouyaud, B.: Annual cycle of energy balance of Zongo Glacier, Cordillera Real, Bolivia, J. Geophys. Res., 104, 3907–3923, 1999.

Wagnon, P., Ribstein, P., Francou, B., and Sicart, J. E.: Anomalous heat and mass balance budget of Glaciar Zongo, Bolivia, during the 1997/98, El Nino year, J. Glaciol., 47, 21–28, 2001.

Wagnon, P., Lafaysse, M., Lejeune, Y., Maisincho, L., Rojas, M., and Chazarin, J. P.: Understanding and modeling the physical processes that govern the melting of snow cover in a

tropical mountain environment in Ecuador, J. Geophys. Res., 114, D19113, doi:10.1029/2009JD012292, 2009.

Wagnon, P., Sicart, J.-E., Berthier, E., and Chazarin, J.-P.: Wintertime high-altitude surface energy balance of a Bolivian glacier, Illimani, 6340 m above sea level, J. Geophys. Res., 108, 4177, doi:10.1029/2002JD002088, 2003.

Wagnon, P., Vincent, C., Arnaud, Y., Berthier, E., Vuillermoz, E., Gruber, S., Ménégoz, M., Gilbert, A., Dumont, M., Shea, J. M., Stumm, D., and Pokhrel, B. K.: Seasonal and annual mass balances of Mera and Pokalde glaciers (Nepal Himalaya) since 2007, The Cryosphere, 7, 1769-1786, doi:10.5194/tc-7-1769-2013, 2013.

Weiers, S.: Zur Klimatologie des NW-Karakoram und angrenzender Gebiete. Statistische Analysen unter Einbeziehung von Wettersatellitenbildern und eines Geographischen Information systems (GIS), Bonner Geographische Abhandlungen, 92, Geographisches Institut, Universitat Bonn, Bonn, Germany, 1995.

Wulf, H., Bookhagen, B., and Scherler, D.: Seasonal precipitation gradients and their impact on fluvial sediment flux in the Northwest Himalaya, Geomorphology, 118, 13–21, 2010.

Yang, W., Guo, X., Yao, T., Yang, K., Zhao, L., Li, S., and Zhu, M.: Summertime surface energy budget and ablation modeling in the ablation zone of a maritime Tibetan glacier, J. Geophys. Res., 116, D14116, doi:10.1029/2010JD015183, 2011.

Zhang, G., Kang, S., Fujita, K., Huintjes, E., Xu, J., Yamazaki, T., Haginoya, S., Wei, Y., Scherer, D., Schneider, C., Yao, T.: Energy and mass balance of the Zhadang Glacier surface, central Tibetan Plateau, J. Glaciol., 213, 137-148, doi:10.3189/2013JoG12J152, 2013.

1

2

3

4 **Table 1.** Measurement specifications for AWS1 located at 4670 m a.s.l. on the mid ablation zone
5 of Chhota Shigri Glacier, AWS2 located on a moraine at 4863 m a.s.l., and precipitation gauge
6 installed at base camp (3850 m a.s.l.). Accumulation/Ablation at AWS1 was measured by SR50A
7 sensor (section 2.3). Variable symbols are also given. Sensor heights indicate the initial distances
8 to the surface (12 August 2012).

Variable	symbol (unit)	Sensor	initial height (m)	stated accuracy
AWS1				
air temperature	T_{air} (^{o}C)	Campbell HMP155A[a]	0.8 & 2.5	±0.1 at 0 ^{o}C
relative humidity	RH (%)	Campbell HMP155A[a]	0.8 & 2.5	±1% RH at 15 ^{o}C
wind speed	u (m s^{-1})	A100LK, Vector Inst.	0.8 & 2.5	±0.1 m s^{-1} up to 10 m s^{-1}
wind direction	WD (degree)	W200P, Vector Inst.	2.5	±2 deg
incoming and outgoing short wave radiations	SWI, SWO (W m^{-2})	Kipp & Zonen CNR-4	1.8	±10% day total
incoming and outgoing long wave radiations	LWI, LWO (W m^{-2})	Kipp & Zonen CNR-4	1.8	±10% day total
air pressure	P_{air} (hPa)	Young 61302V	1	±0.3 hPa
accumulation/ablation	SR50A (m)	Campbell SR50A[b]	1.6[c]	±0.01 m or 0.4% to target
AWS2				
air temperature	T_{air} (^{o}C)	Campbell H3-S3-XT	1.5	±0.1 at 0 ^{o}C
relative humidity	RH (%)	Campbell H3-S3-XT	1.5	±1.5% RH at 23 ^{o}C
wind speed	u (m s^{-1})	Campbell 05103-10-L	3.0	±0.3 m s^{-1}
incoming short wave radiation	SWI (W m^{-2})	Kipp & Zonen CNR-1	2.5	±10% day total
incoming long wave radiation	LWI (W m^{-2})	Kipp & Zonen CNR-1	2.5	±10% day total
Precipitation (base camp)	(mm)	Geonor T-200B	1.7 (inlet height)	±0.6 mm

9 [a] aspirated during daytime with RM Young 43502 radiation shields,
10 [b] mounted on a separate aluminum pole drilled into the ice,
11 [c] 1.6 m was initial height for SR50A sensor
12

13

14

15

16

17

18

19

20

1

2

3

Table 2. Seasonal means and annual mean (standard deviations) of T_{air}, RH, u and SWI over four hydrological years between 1 October 2009 and 30 September 2013 except for LWI (only three years between 1 October 2010 and 30 September 2013) at AWS2 (4863 m a.s.l.). P is the seasonal precipitation for one hydrological year between 1 October 2012 and 30 September 2013 at glacier base camp collected by the Geonor T-200B.

9

	Winter (DJFM)	Pre-monsoon (AM)	Summer-monsoon (JJAS)	Post-monsoon (ON)	Annual mean
T_{air} (°C)	-13.4 (0.9)	-5.3 (0.7)	2.5 (0.6)	-7.8 (1.4)	-5.8 (0.2)
RH (%)	42 (2)	52 (2)	68 (1)	39 (6)	52 (2)
u (m s^{-1})	5.5 (0.6)	3.5 (0.2)	2.8 (0.1)	4.4 (0.5)	4.1 (0.2)
SWI (W m^{-2})	161 (12)	299 (34)	266 (7)	176 (18)	221 (14)
LWI (W m^{-2})	192 (3)	231 (2)	289 (17)	187 (8)	230 (6)
P (mm w.e.)	679	148	117	32	976

10

11

12

13

14

15

16

17

18

19

20

21

22

23

24

1

2

3 **Table 3.** 60-day means (standard deviations) of meteorological and SEB variables measured or
4 computed at AWS1 (4670 m a.s.l.) on Chhota Shigri Glacier for different representative periods.
5 The symbols for variables are described either in the text or in Table 1. SWN, LWN, and R are net
6 short-wave, long-wave and all-wave radiations, respectively.

7

Variable	Post-monsoon (01/10/12-29/11/12)	Winter (01/12/12-29/01/13)	Summer-monsoon (08/07/13-05/09/13)
T_{air} (°C)	-8.6 (2.5)	-14.8 (3.7)	3.6 (1.2)
RH (%)	49 (12)	44 (17)	82 (5)
u (m s^{-1})	4.7 (0.7)	4.9 (1.1)	3.6 (0.5)
STOA (W m^{-2})	276 (39)	216 (11)	458 (25)
SWI (W m^{-2})	175 (46)	130 (44)	248 (67)
SWO (W m^{-2})	127 (31)	101 (32)	47 (15)
α_{acc}	0.73 (0.04)	0.79 (0.04)	0.19 (0.02)
Cloud factor	0.28 (0.26)	0.29 (0.33)	0.36 (0.24)
LWI (W m^{-2})	205 (23)	189 (36)	300 (20)
LWO$_{mod}$ (W m^{-2})	274 (9)	243 (16)	315 (1)
T_{s_mod} (°C)	-9.7 (2.1)	-17.8 (4.3)	-0.2 (0.3)
SWN (W m^{-2})	48 (17)	29 (13)	202 (53)
LWN (W m^{-2})	-69 (19)	-54 (24)	-14 (19)
R (W m^{-2})	-21 (19)	-25 (15)	187 (44)
H (W m^{-2})	10 (13)	28 (23)	31 (10)
LE (W m^{-2})	-45 (9)	-27 (11)	11 (13)
G (W m^{-2})	1 (1)	0 (1)	4 (5)
SW$_{sub}$ (W m^{-2})	-10 (3)	-3 (2)	-40 (11)
H+LE (W m^{-2})	-36 (11)	1 (11)	42 (21)
$F_{surface}$ (W m^{-2})	-56 (16)	-24 (28)	233 (59)
Precipitation (mm w.e. d^{-1})	0.6 (1.0)	5.0 (8.9)	0.5 (0.9)
Snow (mm w.e. d^{-1})	5.3 (5.1)	6.3 (13.0)	1.4 (1.6)
Total melting (mm w.e. d^{-1})	0.6 (1.7)	0.0 (0.0)	61.3 (14.9)
Subl.(-)/re-subl.(+) (mm w.e. d^{-1})[a]	-1.4 (0.3)	-0.8 (0.3)	0.3 (0.4)

8   [a] negative for sublimation, positive for re-sublimation

9

10

41

Table 4. Comparison of SEB components on different glaciers in the High Mountain Asia. All fluxes are in W m^{-2}, Values in brackets are the % contribution of each energy flux.

Glacier	Altitude (m a.s.l.)	Region (ISM dominated, Y or N)	Period of observation	R (W m^{-2})	H (W m^{-2})	LE (W m^{-2})	Rest (W m^{-2})	$F_{surface}$ (W m^{-2})	Reference
Glacier AX010	4960	central Himalaya, Nepal (Y)	25 May- 25 Sep 1978	64 (85)	8 (10)	4 (5)	n/a	74 (100)	Kayastha et al., 1999
Glacier AX010	5080	central Himalaya, Nepal (Y)	25 May- 25 Sep 1978	55 (83)	8(12)	3 (5)	n/a	63 (100)	Kayastha et al., 1999
Xixibangma	5700	south central TP[a] (N)	23 Aug- 11 Sep 1991	28 (200)	5(33)	-19 (133)	n/a	14(100)	Aizen et al., 2002
Parlung No. 4	4800	southeast TP (Y)	21 May- 8 Sep 2009	150 (86)	28 (16)	-1 (1)	-1 (1)	176 (100)	Yang et al., 2011
Zhadang	5660	central TP (N)	1 May - 30 Sep 2010	62 (103)	10 (17)	-8 (13)	-4 (7)	61 (100)	Zhang et al., 2013
Zhadang	5660	central TP (N)	1 May - 15 Sep 2011	27 (117)	8 (35)	-10 (43)	-2 (9)	23 (100)	Zhang et al., 2013
Keqicar	4265	southwest Tianshan (N)	16 June-7 Sep 2005[b]	63 (274)	14 (61)	-54 (235)	n/a	23 (100)	Li et al., 2011
Laohugou No. 12	4550	western Qilian, China (N)	1 June-30 Sep 2011	81 (108)	7 (9)	-13 (17)	n/a	75 (100)	Sun et al., 2014
Chhota Shigri	4670	western Himalaya, India (Y)	8 July-5 Sep 2013	187 (80)	31 (13)	11 (5)	4(2)	230 (100)	Present study

[a]TP = Tibetan Plateau, [b]with a gap of 1 July to7 Aug 2005, n/a = not available
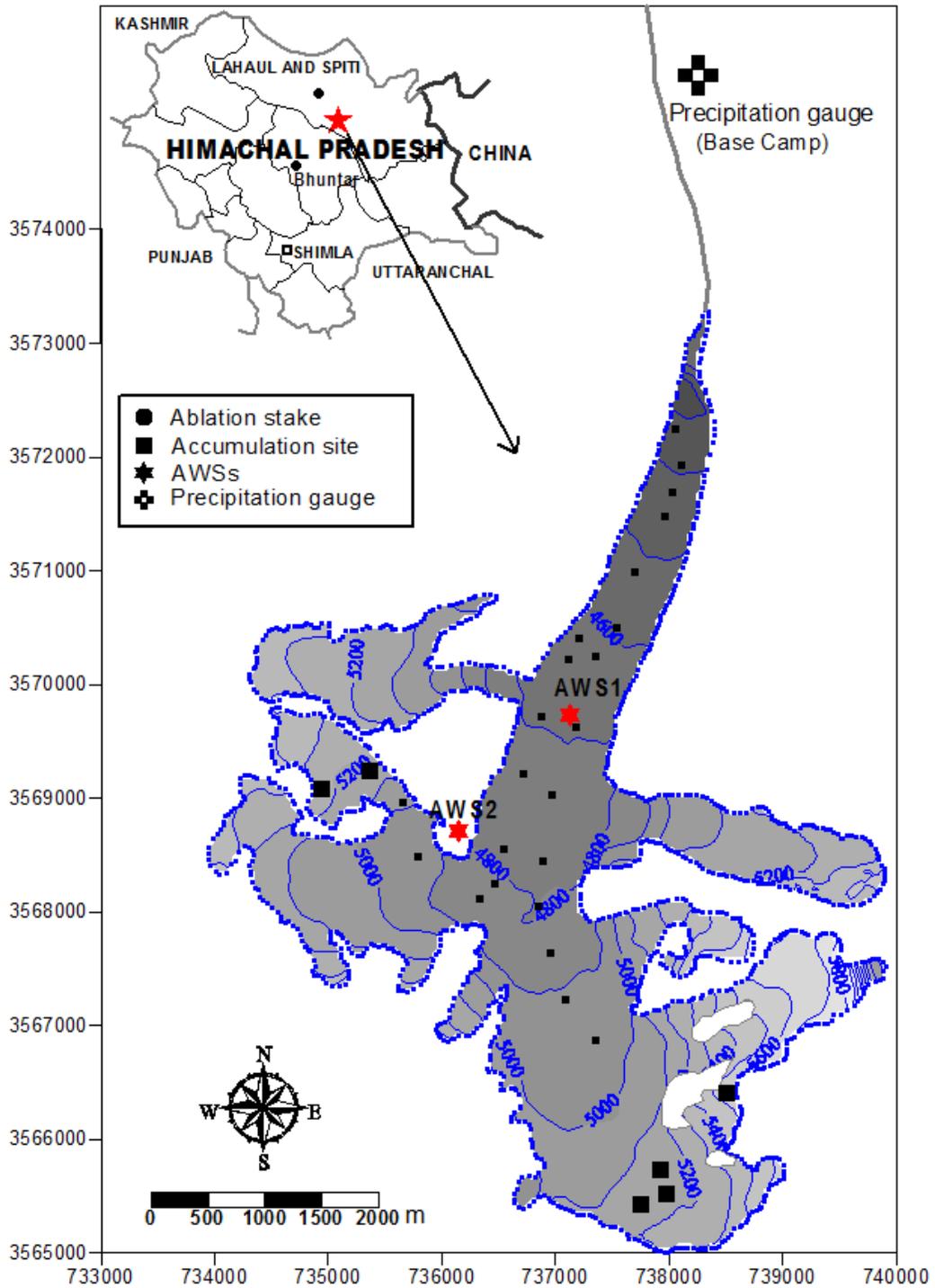
Fig. 1. Map of Chhota Shigri Glacier showing the ablation stakes (black small squares), accumulation sites (black big squares), AWSs (red stars) and precipitation gauge (black cross). The map coordinates are in the UTM43 (north) World Geodetic System 1984 (WGS84) reference system.
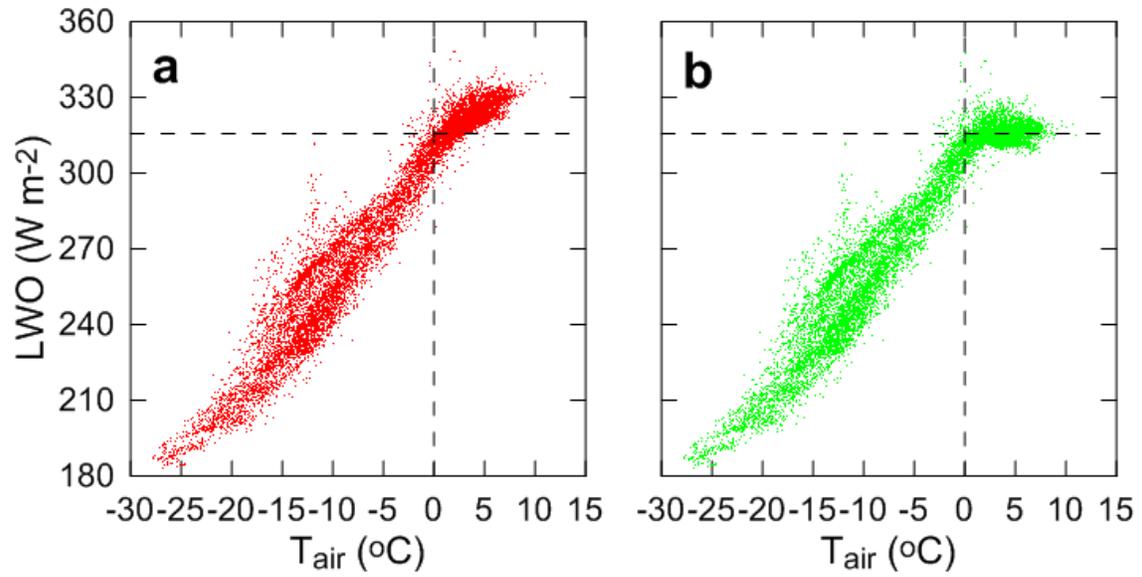
Fig. 2. Half-hourly values of LWO as a function of T_{air}, (a) before and (b) after applying the correction for T_{air} above 0 °C. The dashed lines indicate 0 °C and 315.6 W m^{-2}, the maximum LWO for a melting surface.

Fig. 3. Photographs of AWS1 on Chhota Shigri Glacier taken on 09 October 2012 (left panel) and on 22 August 2013 (right panel) (©: Mohd. Farooq Azam). SR50A mounted on a separate pole drilled into the ice, is visible to the left of AWS1.
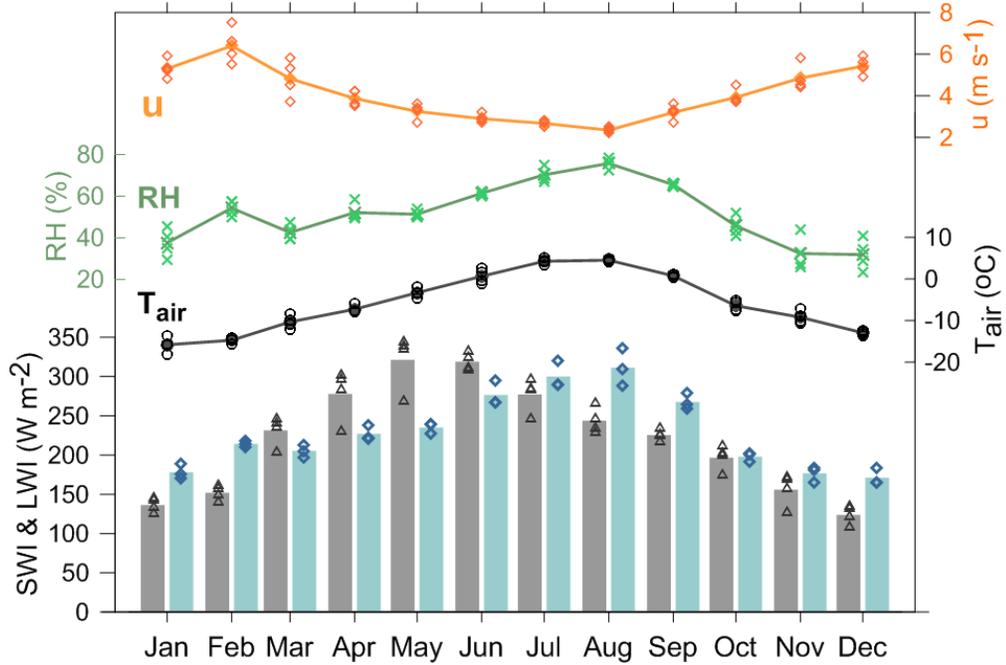
Fig. 4. Mean monthly values of T_{air} (black dots), RH (green crosses), u (orange squares), SWI (grey bars) and LWI (light blue-green bars) at AWS2 (4863 m a.sl.). T_{air}, RH, u and SWI are the mean monthly values of four hydrological years between 1 October 2009 and 30 September 2013 while LWI are the mean monthly values of three hydrological years between 1 October 2010 and 30 September 2013. Also shown are the monthly values of T_{air} (black circles), RH (light green crosses), u (orange hollow squares), SWI (black hollow triangles) and LWI (blue hollow squares) used to derive the mean monthly values.
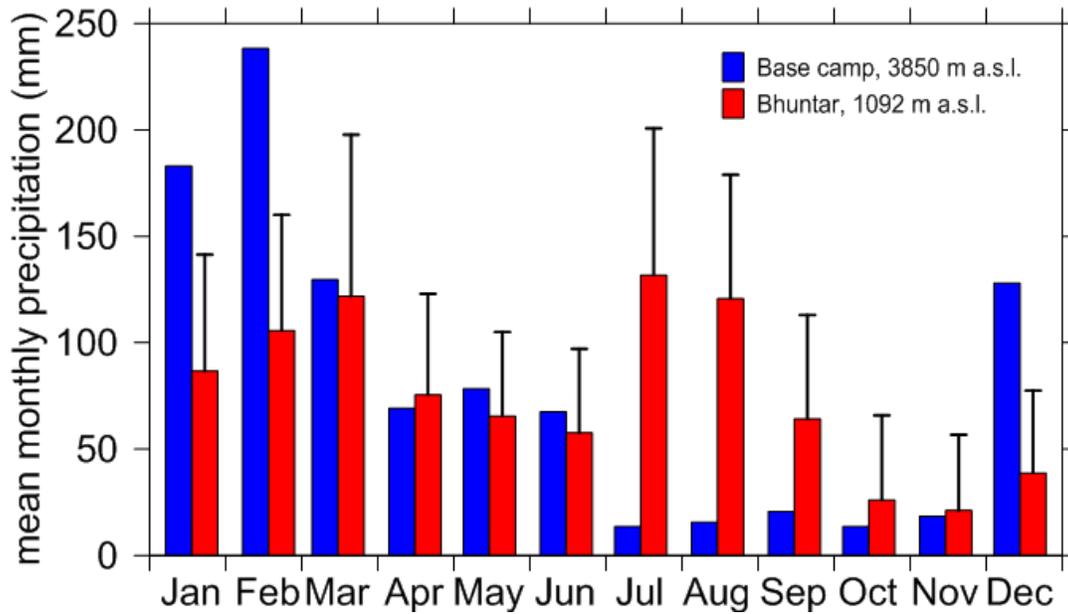
Fig. 5. Comparison of monthly precipitations (blue bars) at Chhota Shigri base camp for 2012/2013 hydrological year with the mean monthly precipitations (red bars) between 1969 and 2013 at Bhuntar meteorological station. The error bars represent the standard deviation (1σ) of the monthly precipitation mean.
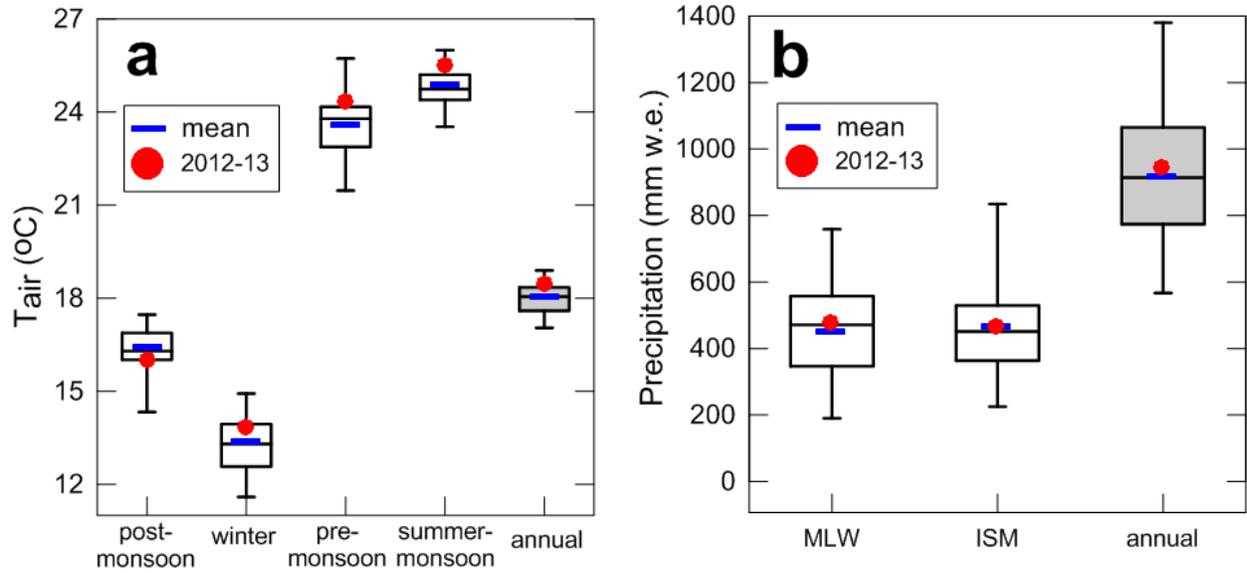
Fig. 6. Boxplots of seasonal and annual T_{air} (a) and precipitation (b) obtained from 44 hydrological years (1969 to 2013) from Bhuntar meteorological station. Boxes cover the 25th to the 75th percentile of each distribution with a central line as the median. The blue thick horizontal line is the 1969-2013 mean, red dot is the 2012/2013 hydrological year mean.
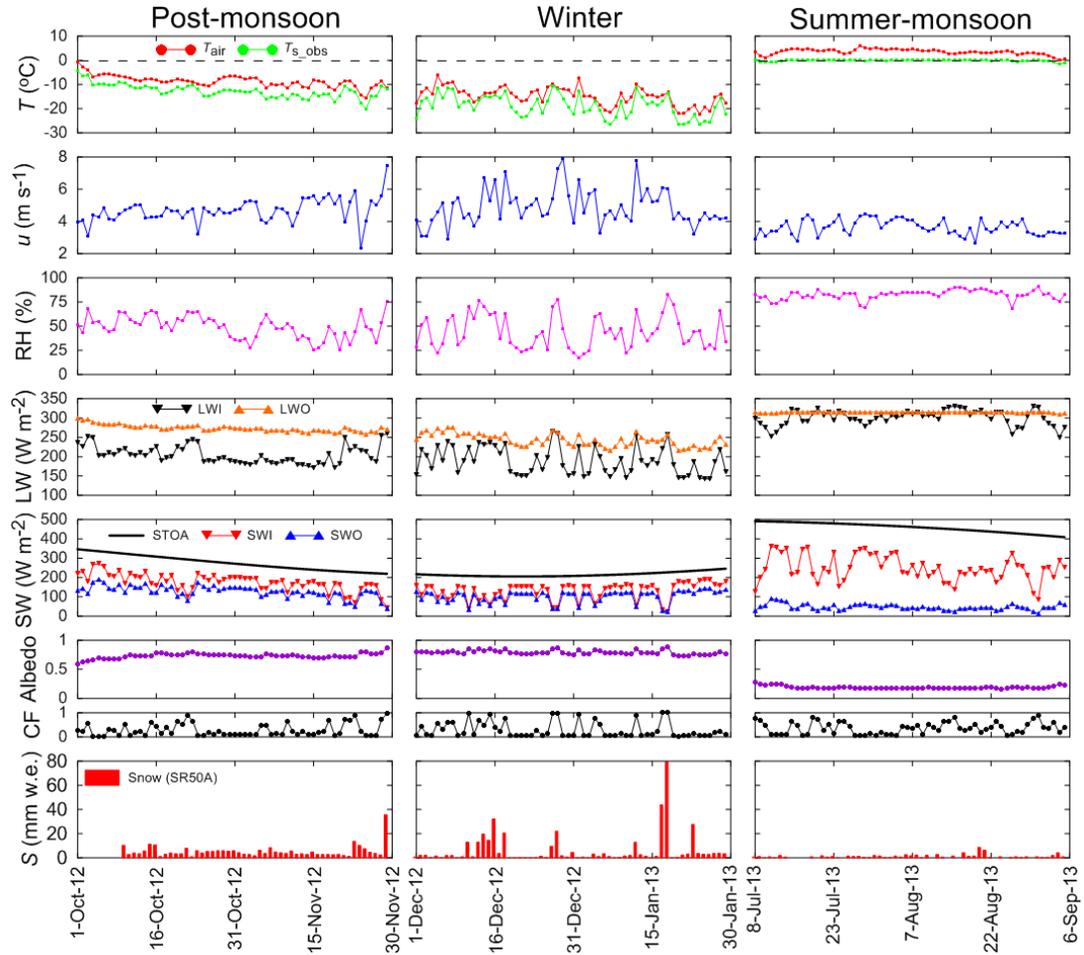
Fig. 7. Daily meteorological variables recorded at AWS1 (4670 m a.s.l.) as representative of post-monsoon (1 October to 29 November 2012), winter (1 December to 29 January 2013) and summer-monsoon (8 July to 5 September 2013) periods. Also shown (lower panel) are the snow falls derived from SR50A data at AWS1.
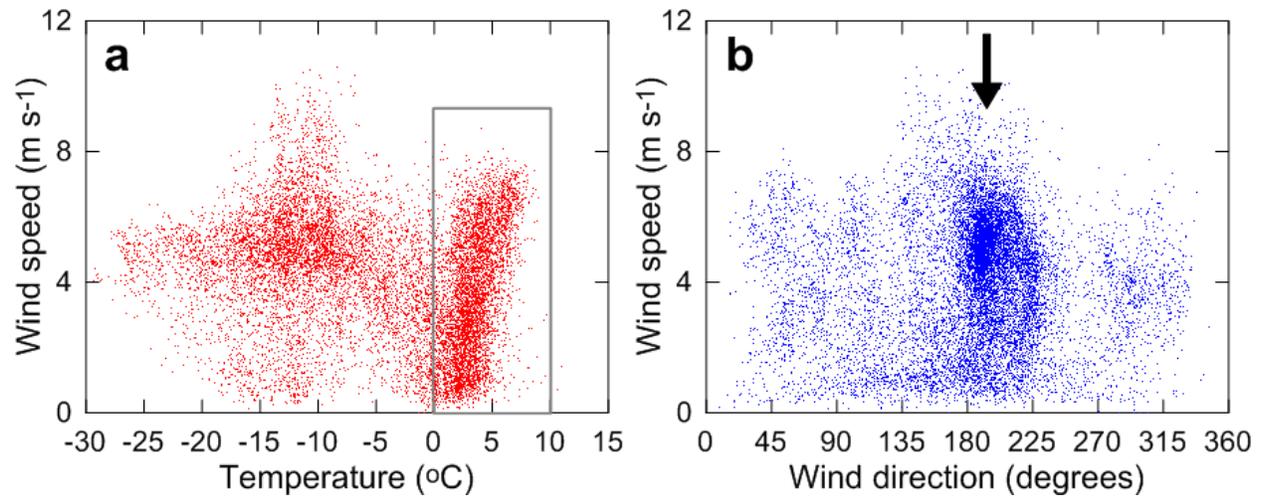
Fig. 8. Scatter plots showing relations between u, T_{air} and WD. In both panels (a and b) all the available measurements are shown, and every dot represents a half-hourly mean value. The inset in (a) highlights the relationship between u and T_{air} above 0 ^{o}C. The arrow in (b) indicates the direction of the local flow line of the glacier.
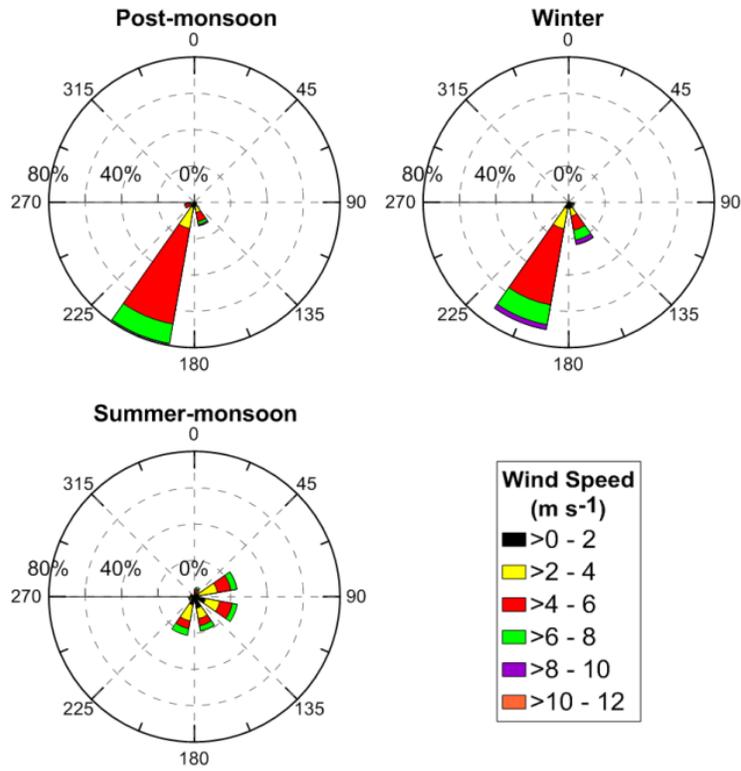
Fig. 9. WD and *u* (half-hourly means) at AWS1 for post-monsoon, winter and summer-monsoon representative periods. The frequency of WD is expressed as percentage over the entire observational period (indicated on the radial axes).
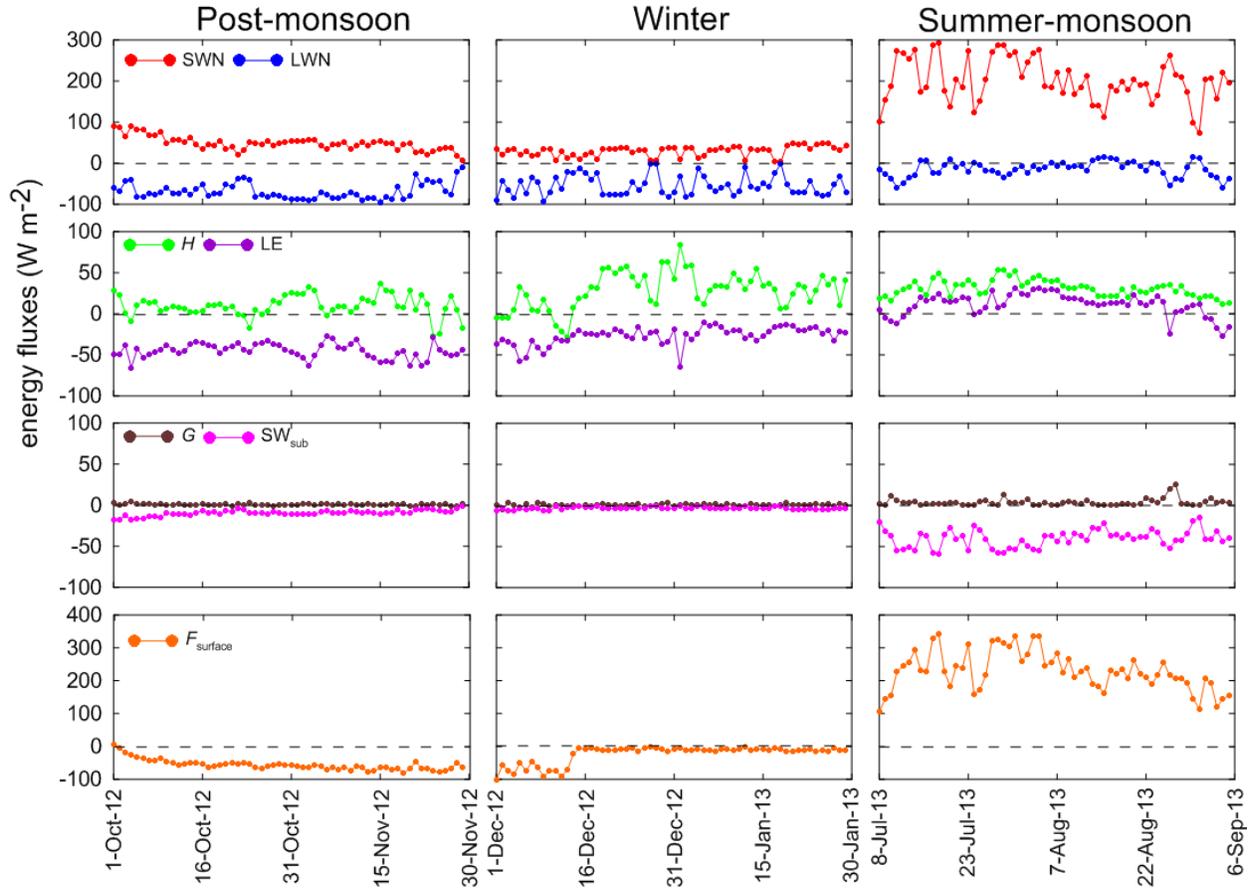
Fig. 10. Daily values of the surface energy fluxes at AWS1 (4670 m a.s.l.) as representative of post-monsoon (1 October to 29 November 2012), winter (1 December to 29 January 2013) and summer-monsoon (8 July to 5 September 2013) periods. SWN, LWN, H, LE, G, SW_{sub} and $F_{surface}$ are the net short-wave radiation, the net long-wave radiation, the turbulent sensible and latent heat fluxes, the conductive heat flux, the short-wave radiation penetrating below the surface, and the amount of energy available at the surface, respectively.
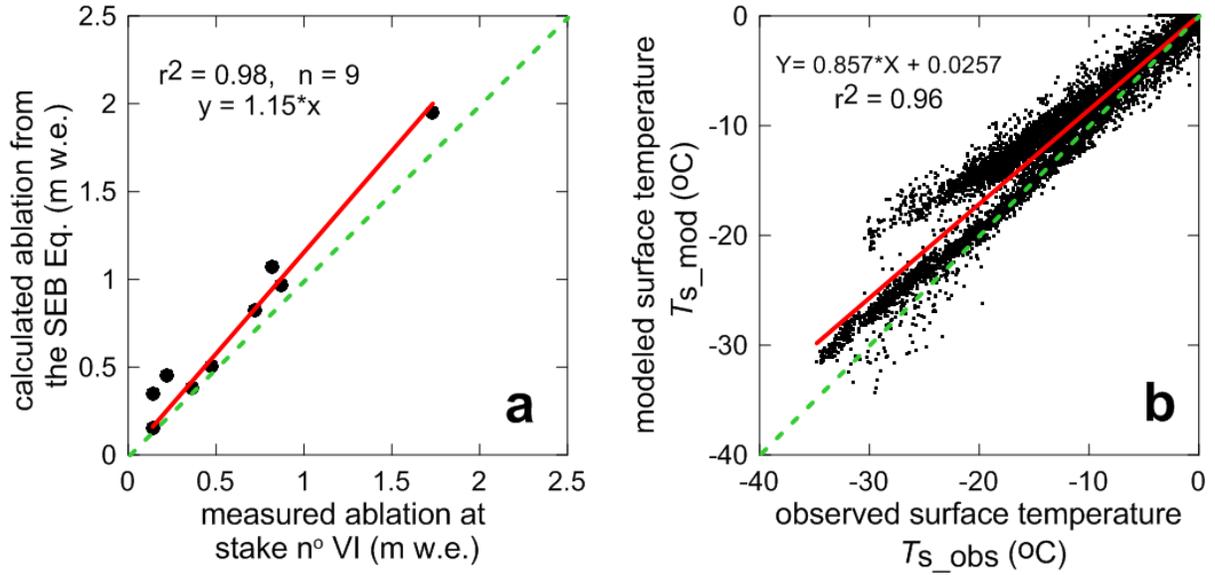
Fig. 11. Comparison between ablation computed from the SEB Eq. and measured at stake n° VI (a) during several few-day to few-week periods of 2012 and 2013 summers where field measurements are available. (b) Comparison between modeled half-hourly ($T_{\text{s\_mod}}$) and observed ($T_{\text{s\_obs}}$) surface temperatures over the whole simulation period. Also shown are the 1:1 line (dashed line) and the regression line (solid line).
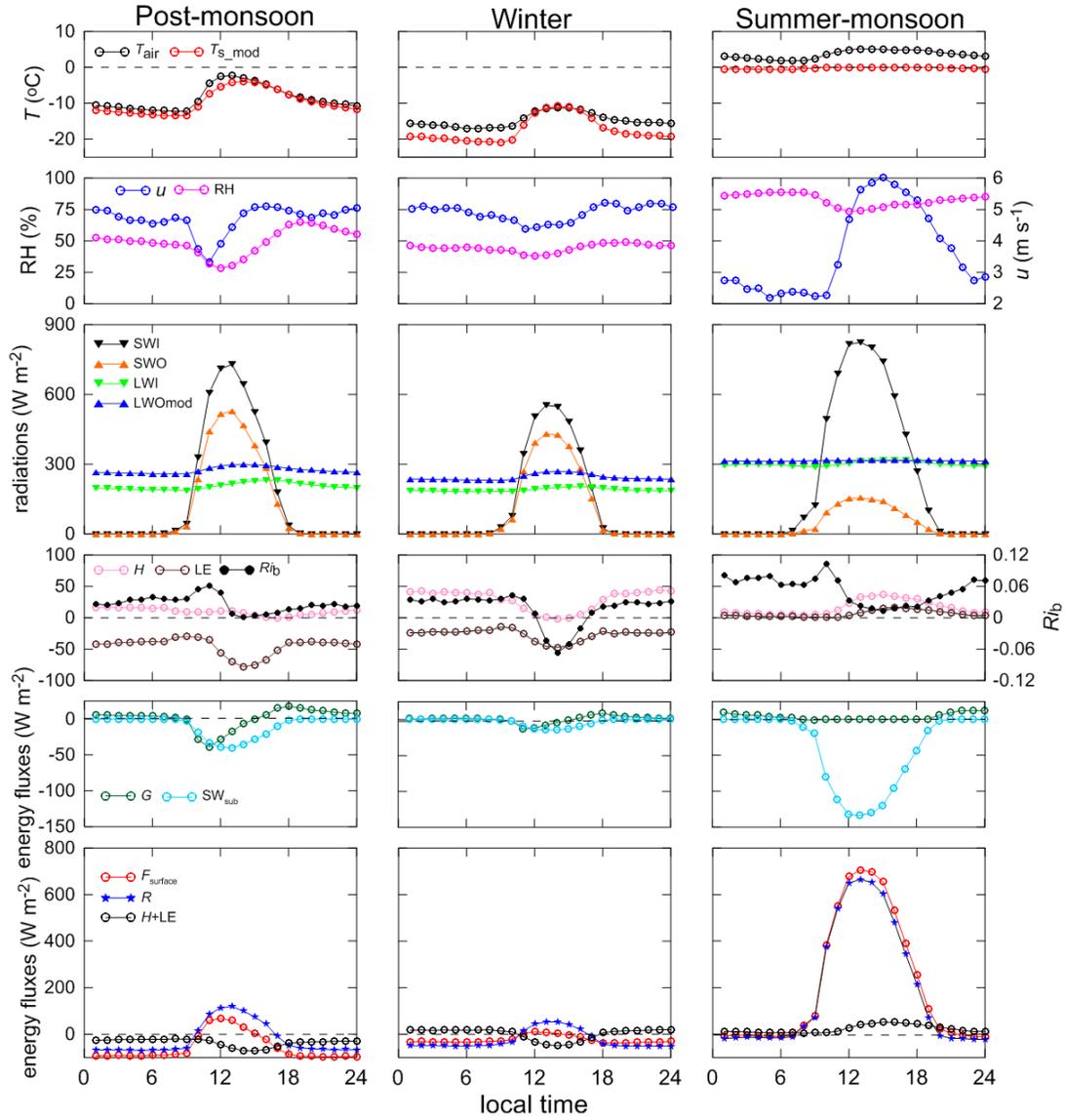
Fig. 12. Mean diurnal cycle of meteorological and SEB variables at AWS1 (4670 m a.s.l.) as representative of post-monsoon (1 October to 29 November 2012), winter (1 December to 29 January 2013) and summer-monsoon (8 July to 5 September 2013) periods.
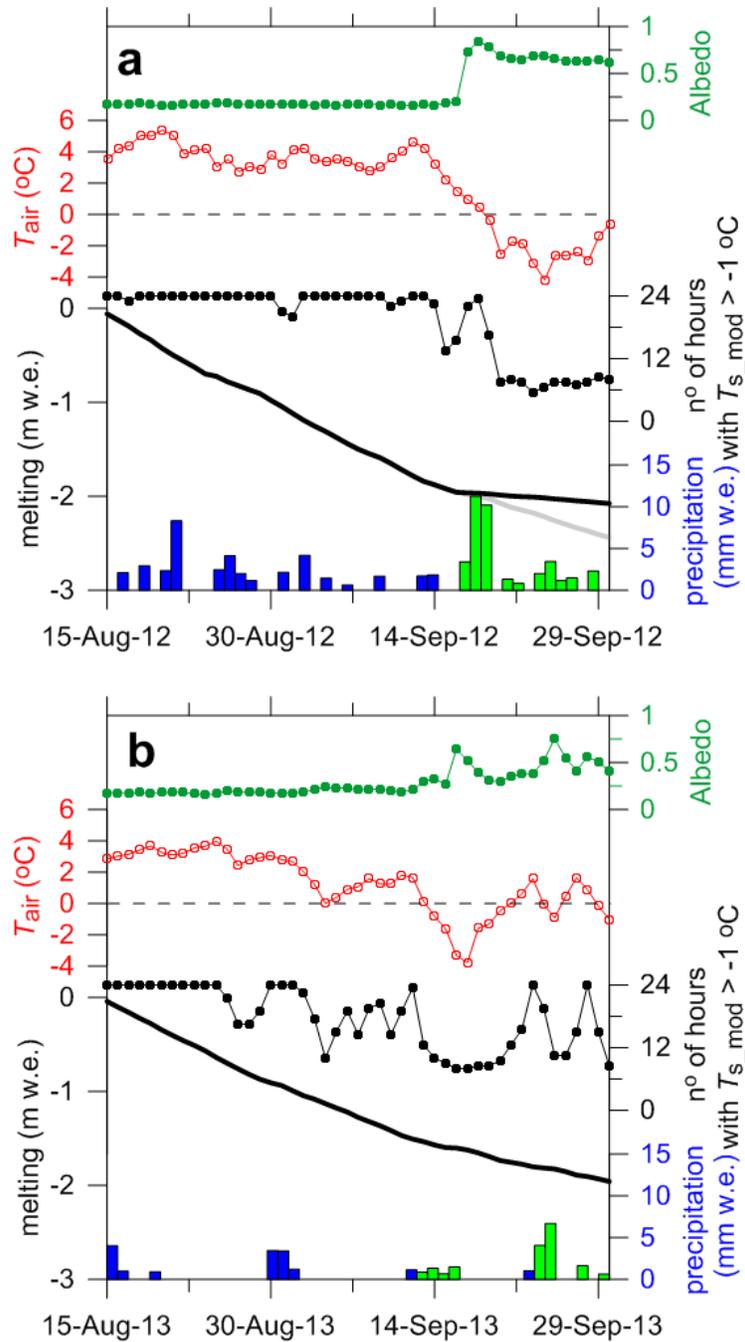
Fig. 13. Comparison of computed cumulative melting (black thick line) between 15 August and 30 September from summers 2012 (a) and 2013 (b). Also shown are the mean T_{air} (red open dots), the number of hours in a day when T_{s_mod} is > -1 °C (black dots), daily albedo (dark green dots) and the precipitations as rain/snow obtained from records at base camp (blue and green bars, respectively). The grey line in panel (a) is the computed cumulative melting between 15 August and 30 September 2012 assuming a constant surface albedo of 0.19.
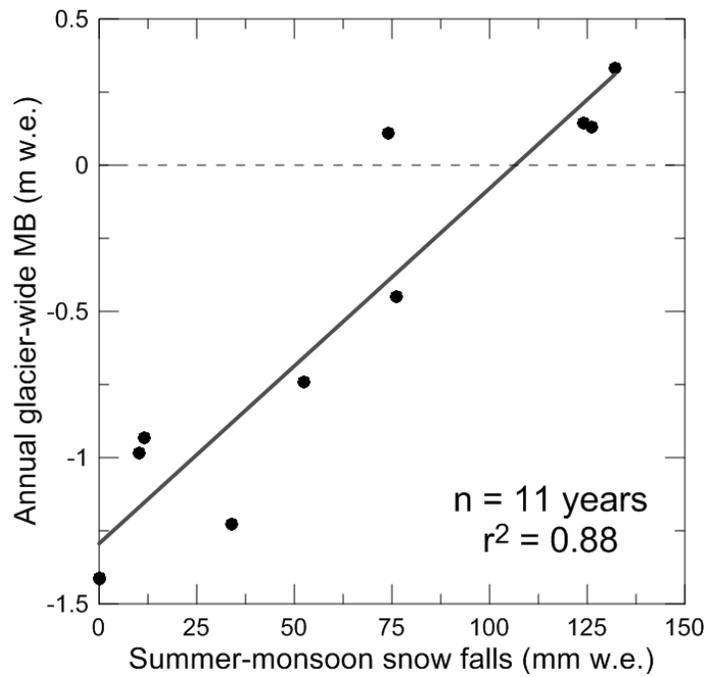
Fig. 14 Annual glacier-wide mass balance as a function of the sum of the 3 largest summer-monsoon daily snowfalls assessed from precipitation record from Bhuntar meteorological station (see text for details) between 2002 and 2013.